Factors Affecting the Rapid Recovery of CAPE on 31 March 2016 during VORTEX-Southeast

ALLISON T. LAFLEUR,[a] ROBIN L. TANAMACHI,[a] DANIEL T. DAWSON II,[a] AND DAVID D. TURNER[b]

[a] *Department of Earth, Atmospheric, and Planetary Sciences, Purdue University, West Lafayette, Indiana*
[b] *NOAA/Global Systems Laboratory, Boulder, Colorado*

(Manuscript received 23 February 2022, in final form 27 February 2023, accepted 28 February 2023)

ABSTRACT: In this study, we analyze various sources of CAPE in the environment and their contributions to its time tendency that will complement forecast models and operational analyses that are relatively temporally (~1 h) coarse. As a case study, the relative roles of direct insolation and near-surface moisture advection in the recovery CAPE on 31 March 2016 in northern Alabama are examined using VORTEX-Southeast (VORTEX-SE) observations and numerical simulations. In between rounds of nontornadic morning storms and tornadic evening storms, CAPE over the VORTEX-SE domain increased from near zero to at least 500 J kg^{-1}. A timeline of the day's events is provided with a focus on the evolution of the lower levels of the atmosphere. We focus on its responses to solar insolation and moisture advection, which we hypothesize as the main mechanisms behind the recovery of CAPE. Data from the University of Massachusetts S-Band frequency-modulated, continuous-wave (FMCW) radar and NOAA National Severe Storms Laboratory (NSSL) Collaborative Lower Atmospheric Mobile Profiling System (CLAMPS), and high-resolution EnKF analyses from the Advanced Regional Prediction System (ARPS) are used to characterize the boundary layer evolution in the pre-tornadic storm environment. It is found that insolation-driven surface diabatic heating was the primary driver of rapid CAPE recovery on this day. The methodology developed in this case can be applied in other scenarios to diagnose the primary drivers of CAPE development.

SIGNIFICANCE STATEMENT: The mechanisms by which atmospheric instability recovers can vary widely and are often a source of uncertainty in forecasting. We want to understand how and why the environment destabilized enough to produce an evening tornado following morning storms on 31 March 2016. To do this, we used model data and observations from a collocated radar and profiler. It was found that heating from the sun at the surface was the primary cause of destabilization in the environment.

KEYWORDS: CAPE; Convective storms; Mesoscale processes; Storm environments

1. Introduction

Tornadoes in the southeast (SE) region of the United States can occur under different conditions than are typically seen in the Southern Great Plains (SGP) region. For instance, in the SE United States, tornadic storms have been observed to form and persist when analyzed CAPE is less than 500 J kg^{-1} provided sufficient shear is also present; this is the so-called "high shear, low CAPE" (HSLC) regime (Sherburn and Parker 2014; Anderson-Frey et al. 2016; Sherburn et al. 2016; King et al. 2017). Such low-CAPE tornadic storms are most common during the cold season (Childs et al. 2018) or at night (Kis and Straka 2010; Sherburn and Parker 2014; Ashley 2007). While these environments and associated storms can occur anywhere, the SE United States experiences a relatively high fraction of these apparent low-CAPE storms and is therefore at greater risk from them. Another difficulty with standard mesoscale analyses, specifically the SPC mesoanalysis, is that their relatively coarse temporal resolution (typically 1 h) may miss situations where CAPE can increase abruptly owing to rapid (<1 h) destabilization of the environment (Hart et al. 2016; King et al. 2017). The desire for subhourly resolution is part of the motivation of the present study. The goals of the present study are to assess the inaccuracies in CAPE analyses in such rapid-recovery situations that stem directly from inadequate temporal resolution, as well as to understand the physical mechanisms responsible for the rapid CAPE recovery. We will examine the time evolution of CAPE and its sources preceding an outbreak of severe storms on 31 March 2016 in northern Alabama (AL) that occurred during the Verification of the Origin of Rotation in Tornadoes Experiment-Southeast (VORTEX-SE) field program (Rasmussen et al. 2015; Koch and Rasmussen 2016).

VORTEX-SE is an ongoing research program to study tornadoes and tornado environments in the SE United States. Its stated objectives include understanding the environments of the SE United States that influence the structure and path of the region's tornadoes, as well as how to best communicate warnings of these storms to the public (Rasmussen et al. 2015). The tornadoes in the SE United States often occur at night, in forested areas, and/or outside of the perceived tornado season. Additionally, they often occur in areas with limited visibility, inadequate shelter, and/or a large population. These factors are believed to contribute to the disproportionately large number of killer tornadoes in this area (Ashley 2007), making the accurate assessment of tornadic potential in storms of high importance.

Corresponding author: Allison LaFleur, alafleu@purdue.edu

DOI: 10.1175/MWR-D-22-0051.1

© 2023 American Meteorological Society. For information regarding reuse of this content and general copyright information, consult the AMS Copyright Policy (www.ametsoc.org/PUBSReuseLicenses).

Brought to you by NOAA Central Library | Unauthenticated | Downloaded 08/02/23 01:52 PM UTC

TABLE 1. Meteorological variables with their corresponding instrument and sampling height from the meteorological tower at Belle Mina, AL (Lee et al. 2016a).

Variable	Instrument	Sampling height(s) (m AGL)
Temperature, dewpoint temperature	Vaisala HMP110 humidity and temperature probe	1.5
Temperature	Platinum resistance thermometer (PRT) in aspirated shield	3, 10
Net radiation	Hukseflux 4-component net radiometer	2.5

In this study, we apply the methods of Emanuel (1994) and Agard (2017) to examine various sources of CAPE in the environment and their contributions to its time tendency that will complement forecast models and operational analyses that are relatively temporally (~1 h) coarse. We apply this technique to a low-CAPE tornadic storm case from VORTEX-SE on 31 March 2016 in northern Alabama to determine the relative importance of CAPE sources prior to the development of a tornadic storm with a focus on the temporal evolution. We evaluated the rate of convective destabilization and its causes using a combination of VORTEX-SE observations (Rasmussen and Koch 2016) and EnKF-based numerical analyses. We focus our analysis on Belle Mina because our main instruments, the University of Massachusetts (UMass) S-Band frequency-modulated, continuous-wave (FMCW) radar and NOAA National Severe Storms Laboratory (NSSL) Collaborative Lower Atmospheric Mobile Profiling System (CLAMPS; Wagner et al. 2019), were collocated there.

2. Data and methodology

a. Observation data

In addition to the UMass radar and the CLAMPS ATDD also participated in VORTEX-SE and operated a 10-m meteorological tower at Belle Mina. This tower collected meteorological, soil, and vertical flux observations (Lee et al. 2016a), of which we used surface temperature T, dewpoint T_d, and net radiation R. Table 1 details the instruments on the tower that we utilized. The tower sampled data every 5 s and reported the 30-min mean, except for the sonic anemometers and gas analyzers that sampled at 10 Hz (Lee et al. 2016a).

The Collaborative Lower Atmospheric Mobile Profiling System (CLAMPS; Geerts et al. 2017; Wagner et al. 2019) provided boundary layer profiles of temperature T and dewpoint temperature T_d at times intermediate to those of the soundings. The Atmospheric Emitted Radiance Interferometer (AERI; Knuteson et al. 2004a,b), which is one of the principal instruments of the CLAMPS, is an operational ground-based infrared spectrometer that measures the downwelling infrared (3–19 μm) radiance emitted by the atmosphere at a high temporal (~1 s) and spectral (cm^{-1}) resolution. The AERI observations in the 15-μm carbon dioxide band and the 18-μm water vapor band are used to infer profiles of temperature and water mixing ratio, respectively.

The optimal estimation-based approach of Turner and Löhnert (2014) and Turner and Blumberg (2019) is used to invert the AERI radiance data, constrained by a climatological radiosonde dataset, to provide the retrieved thermodynamic profiles with their uncertainties (known as "AERIoe" profiles). This retrieval technique has been evaluated against radiosondes in multiple locations and seasons, demonstrating that the AERI has a good ability to characterize the evolution of the boundary layer (Blumberg et al. 2015; Wulfmeyer et al. 2015; Klein et al. 2015; Weckwerth et al. 2016; Turner and Blumberg 2019). A study of the accuracy of CAPE derived from AERI-retrieved profiles demonstrated that the remotely sensed CAPE was able to accurately capture destabilization trends (Blumberg et al. 2017). The convective boundary layer profiles CAPE calculations from the AERI had correlation coefficients above 0.92 when compared with those calculated from collocated soundings. Additionally, during the daytime MLCAPE was the most accurate and during the night SBCAPE was the most accurate. However, all the correlations, as mentioned above, were high (>0.9) and therefore useful.

The AERI does have some limitations compared to radiosondes due to being a passive instrument. For our data the vertical resolution of the AERI ranges from 70 to 200 m at the surface to a little over 3 km at the top for the water vapor and about 6 m to 4–5 km at the top for temperature. While it still has a lower vertical resolution than radiosondes it has been found that by supplementing the AERI profiles with data from the mid- to upper troposphere, destabilization trends can be identified (Blumberg et al. 2017). We supplemented our AERI calculated soundings in this study with sounding data from the NOAA/ATDD group, and then calculated CAPE from the soundings and AERIoe profiles (Fig. 1, Table 2).

Unless otherwise specified, we used MetPy (May et al. 2021) for the calculations of CAPE and related quantities in this study. MetPy is an open-source, Python-based library that contains methods to calculate and plot soundings and associated thermodynamic and kinematic parameters given vertical profiles of temperature, dewpoint, pressure, height, wind speed, and wind direction.

b. Numerical modeling

Many of the quantities required to compute the terms in the CAPE tendency equation were either not available or are otherwise difficult or impossible to obtain from the single-site observation platforms in our study. These include information on horizontal and vertical advective tendencies and surface sensible and latent heat fluxes. Therefore, we utilized a numerical model to compute these quantities. We used the Advanced Regional Prediction System (ARPS; Xue et al. 2000, 2001) coupled with an EnKF-based data assimilation system

Brought to you by NOAA Central Library | Unauthenticated | Downloaded 08/02/23 01:52 PM UTC

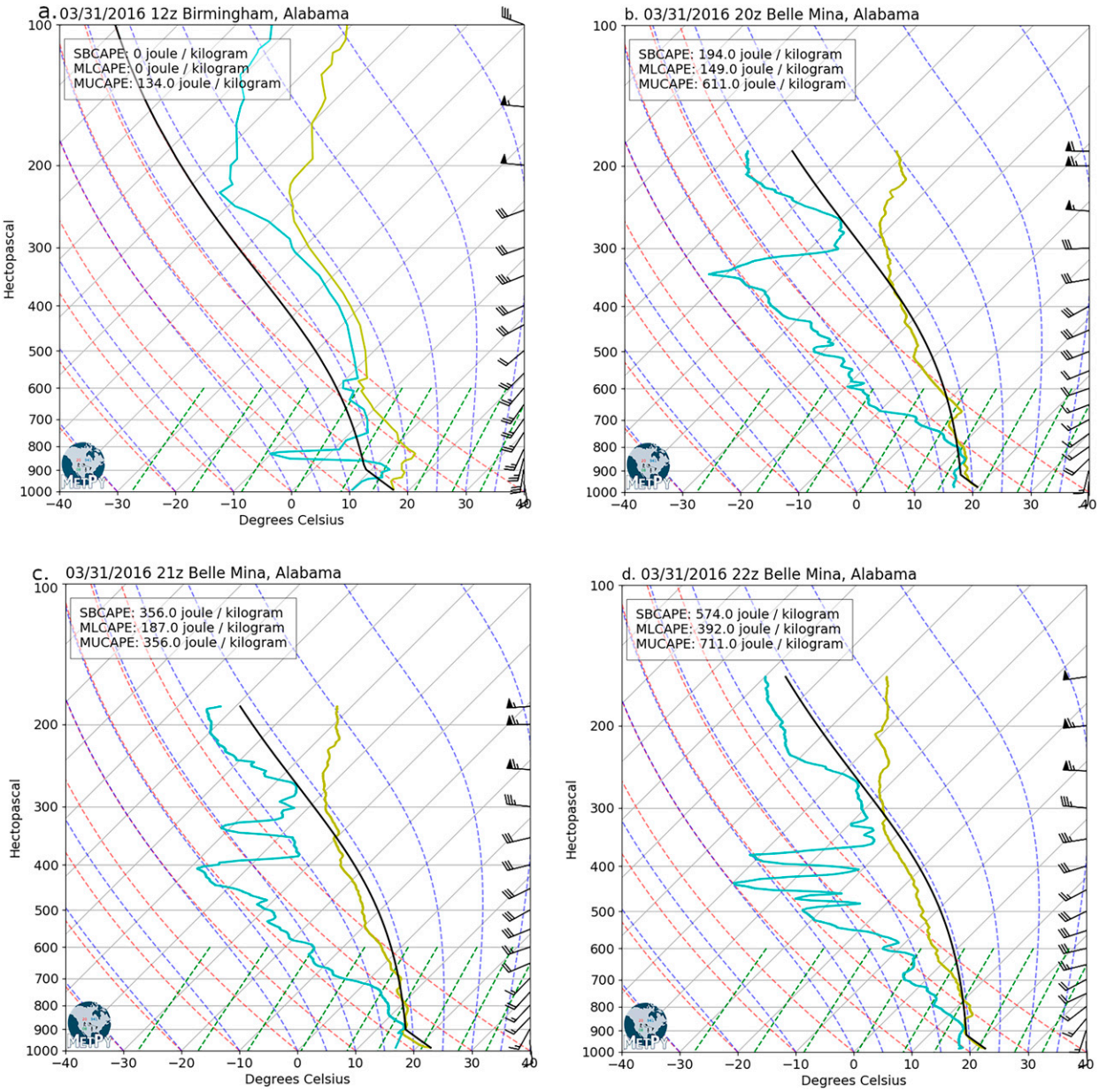

FIG. 1. Skew T–log$p$ plots of the radiosonde soundings from (a) 1200 UTC at Birmingham, AL; (b) 2000 UTC at Belle Mina, AL; (c) 2100 UTC at Belle Mina, AL; and (d) 2200 UTC 31 Mar at Belle Mina, AL. The yellow trace shows the temperature, and the cyan trace shows the dewpoint (°C); the black line shows the surface parcel trajectory. Dashed red and blue contours are dry and moist adiabats, respectively, and dashed green contours are isohumes of saturation mixing ratio. The winds are in m s^{-1}.

(ARPS-EnKF; Tong and Xue 2005; Dawson et al. 2013) with 40 ensemble members to model the atmospheric conditions over the VORTEX-SE domain on 31 March 2016. In addition to the benefits afforded by the EnKF in regard to generating accurate mean analyses, by utilizing the ensemble of model states we can additionally obtain information regarding the uncertainty in the various factors affecting the development of CAPE in the region. The ARPS is a nonhydrostatic numerical cloud model designed to be used on the regional-to-storm scale (Xue et al. 2000, 2001). We used a telescoping one-way nested domain configuration centered over northern Alabama with an outer 1800 × 1800 km^2 grid at 6-km grid spacing and an inner 450 × 450 km^2 grid at 3-km grid spacing (Fig. 2). The outer 6-km grid used initial and boundary conditions (including soil moisture and temperature) interpolated from the 0600 UTC North American Mesoscale Forecast System (NAM; Janjić 2003) with 12-km grid spacing. We generated a set of 40 ensemble members from this interpolated NAM analysis by applying random Gaussian perturbations smoothed with a 2D recursive filter (Tong and Xue 2008; Jung et al. 2012) with

Brought to you by NOAA Central Library | Unauthenticated | Downloaded 08/02/23 01:52 PM UTC

TABLE 2. Surfaced-based, mixed-layer, and most-unstable CAPE and CIN (J kg^{-1}) from three ATDD radiosonde soundings taken at Belle Mina, AL, on 31 Mar 2016 (Lee et al. 2016b).

Time (UTC)	2000	2100	2200
SBCAPE	194.0	356.0	574.0
SBCIN	−51.0	0.0	0.0
MLCAPE	149.0	187.0	392.0
MLCIN	0.0	−61.0	0.0
MUCAPE	611.0	356.0	711.0
MUCIN	−67.0	0.0	−65.0

correlation length scales of 36 km in the horizontal and 7.2 km in the vertical to the model potential temperature, water vapor specific humidity, and horizontal wind component fields. The inner 3-km grid used initial and boundary conditions from the parent 6-km grid at 5-min intervals. The simulation period started at 0600 UTC 31 March with an initial 6-h free-forecast "spinup period" on the 6-km grid assimilating conventional surface observations every 15 min using the ARPS-EnKF until 0300 UTC 1 April. The 3-km experiment was initialized from the 6-km ensemble analysis at 1200 UTC and assimilated conventional surface observations and reflectivity and radial velocity data from area NEXRAD radars (cf. Fig. 2) at 15-min intervals until 0300 UTC. Covariance cutoff radii of 300 and 6 km in the horizontal and vertical, respectively, were applied to assimilated surface observations, while a radius of 6 km was used in both the horizontal and vertical for radar data. To maintain ensemble spread, a combination of multiplicative inflation (Anderson 2001) with a factor of 1.2 applied in regions of reflectivity > 5 dBZ and adaptive relaxation to prior spread (RTPS; Whitaker and Hamill 2012) with a factor of 0.9 were used. The model parameterization configuration included a nonlocal PBL parameterization based on a 1.5-order TKE scheme (Xue et al. 1996, 2003) and the triple-moment version of the NSSL precipitation microphysics scheme (Mansell et al. 2010; Dawson et al. 2014). No convective parameterization was used on either of the grids. A two-layer land surface model based on Noilhan and Planton (1989) and Pleim and Xiu (1995) was used, with stability-dependent drag coefficients computed for the surface fluxes. The radiation scheme for surface long- and shortwave fluxes and atmospheric heating rates was based on the NASA Goddard Space Flight Center scheme (Chou 1990, 1992; Chou and Suarez 1994).

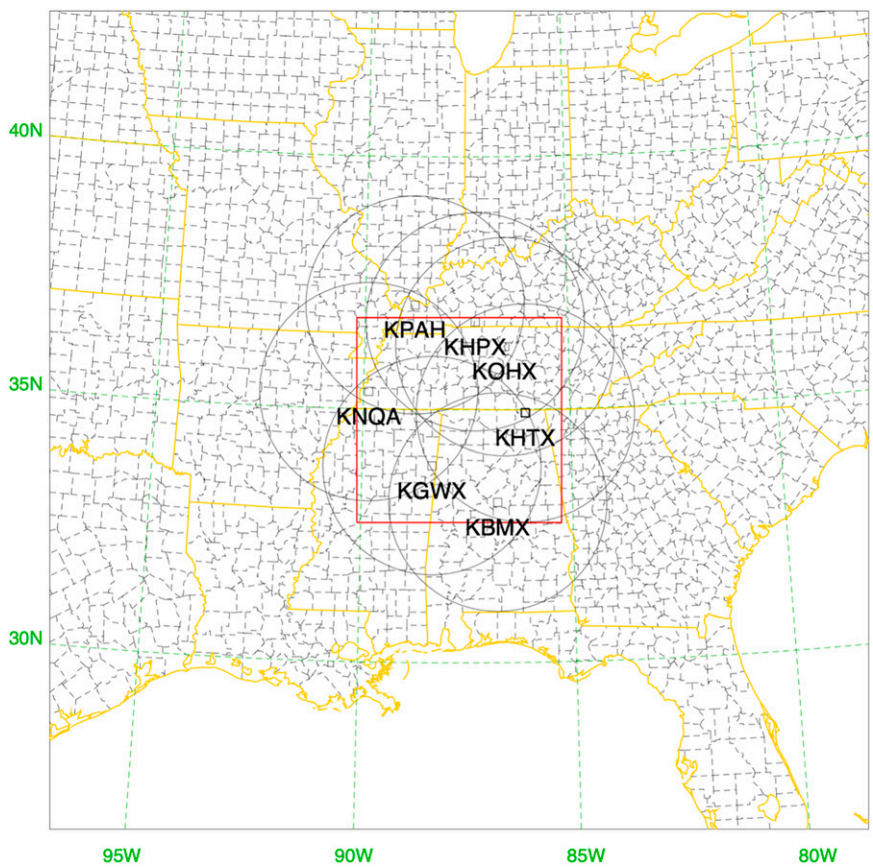

FIG. 2. Configuration for the outer 6-km (black bounding box) and inner 3-km (red box) ARPS-EnKF domains. Also shown are the NEXRAD radars assimilated on the 3-km grid with 240-km range rings for reference.

Brought to you by NOAA Central Library | Unauthenticated | Downloaded 08/02/23 01:52 PM UTC

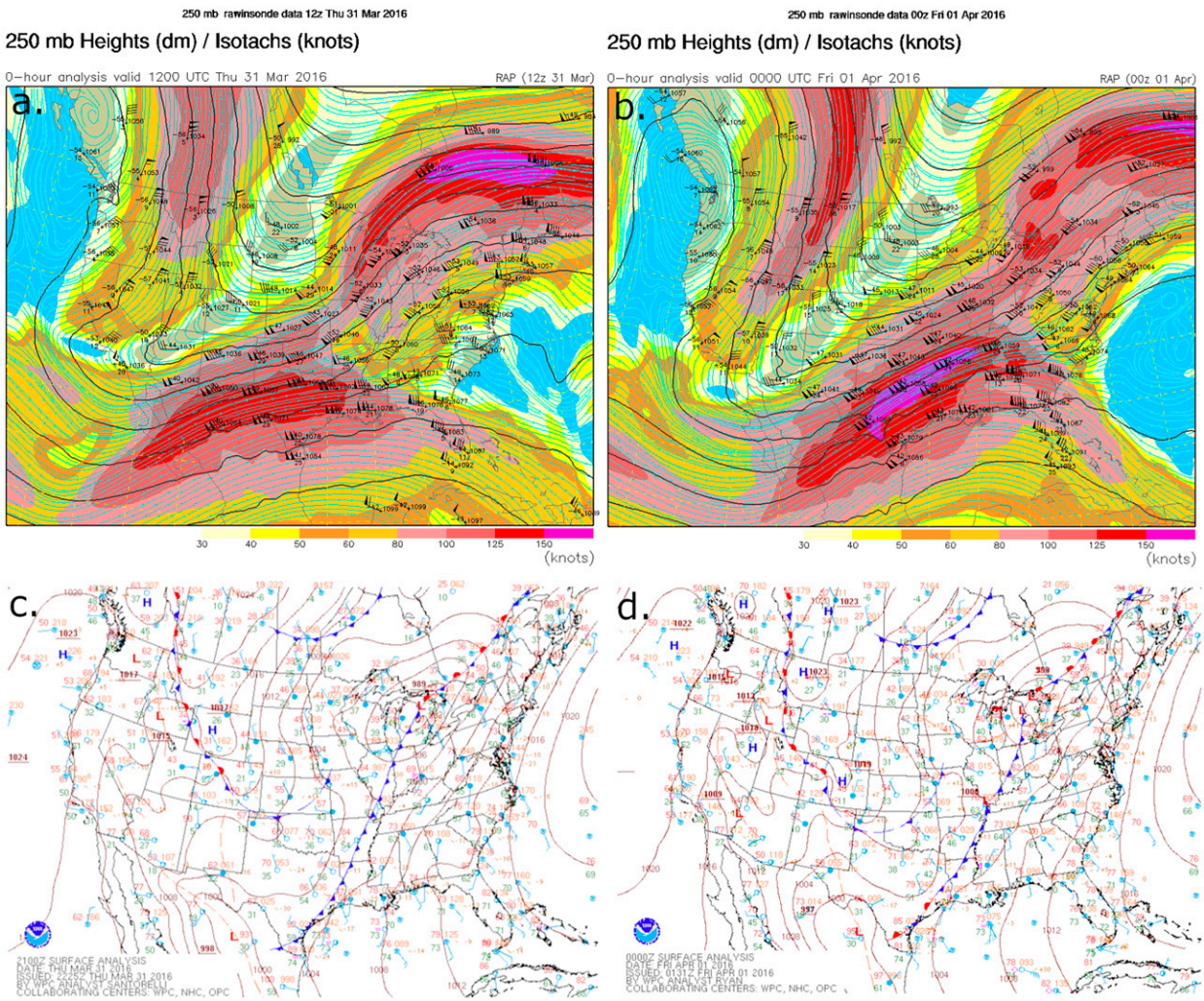

FIG. 3. Analyzed 250-mb (1 mb = 1 hPa) heights and winds at (a) 1200 UTC 31 Mar 2016 and (b) 0100 UTC 1 Apr 2016 and surface analysis from (c) 2100 UTC 31 Mar 2016 and (d) 0000 UTC 1 Apr 2016. Panels (a) and (b) are courtesy of UCAR; panels (c) and (d) are from the NWS Weather Prediction Center.

c. *Time tendency of CAPE calculation*

Following Emanuel (1994) and Agard (2017), we write the following equation for the time tendency of CAPE:

$$\frac{d}{dt}\mathrm{CAPE}_i \approx \underbrace{(T_i - T_{\mathrm{EL}})\frac{ds_i}{dt}}_{\text{Term A}} - \int_{z_{\mathrm{LFC}}}^{z_{\mathrm{EL}}}\left[\underbrace{\frac{g\dot{Q}}{c_p T}}_{\text{Term B}} - \underbrace{\frac{g}{\theta}(\mathbf{v}\cdot\nabla\theta)}_{\text{Term C}}\right]dz, \tag{1}$$

where the subscripts i, LFC, and EL represent the parcel source level, and the parcel's level of free convection and equilibrium level, respectively. The term T is the temperature, θ is the potential temperature, s is specific entropy, c_p is the specific heat at constant pressure, g is the acceleration due to gravity, $\dot{Q}$ is the radiative heating rate (J kg^{-1} s^{-1}) and $\mathbf{v}$ is the 3D wind vector relative to the parcel motion at source level. For simplicity, we take the parcel source level to be that of the first level above ground (i.e., the "surface" parcel); therefore, the CAPE calculated from (1) is SBCAPE, and will be denoted as such from this point onward when analyzing the terms in (1). Since we are concerned with the CAPE tendency at a fixed column (over the Belle Mina site), the parcel being lifted is fixed relative to the ground, and v in our case is therefore simply the ground-relative wind vector. Finally, in our analysis, we neglect the effects of water vapor on parcel buoyancy (i.e., the "virtual temperature correction"; Doswell and Rasmussen 1994) owing to potential issues with this correction in MetPy at the time of this writing. However, these effects could be included by using the virtual temperature/potential temperature in place of the regular versions in (1). To evaluate (1), we require the vertical profiles of temperature and potential temperature, wind, and radiative heating rates, as well as the parcel LFC and EL heights. As described in more detail below, we computed the terms in (1) from the

Brought to you by NOAA Central Library | Unauthenticated | Downloaded 08/02/23 01:52 PM UTC

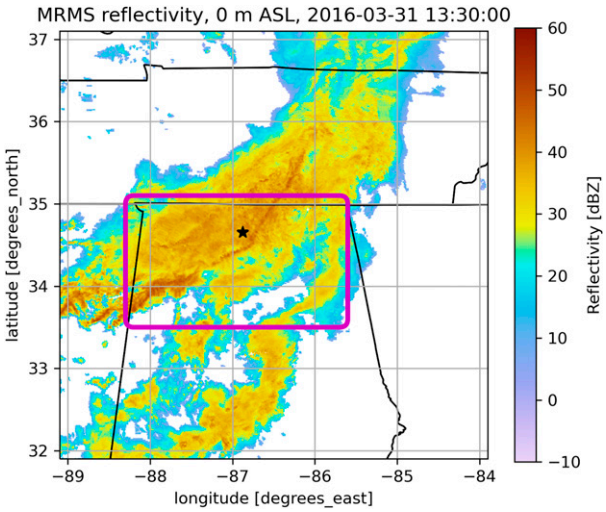

FIG. 4. MRMS reflectivity mosaic (dBZ) at 0 m MSL at 1330 UTC 31 Mar 2016, depicting the morning storms passing over the Belle Mina, AL, observation site (black star) from west to east. The magenta box encompasses the VORTEX-SE domain. Radar image created using Py-ART (Helmus and Collis 2016).

ARPS ensemble model output and integrated them using the trapezoidal rule at 5-min intervals to quantify each term's cumulative contribution to SBCAPE at the Belle Mina site.

In Eq. (1), Term A represents the change in SBCAPE owing to changes in the entropy of the parcel source layer. In our case, this is the surface, but this term also represents the boundary layer entropy change for a well-mixed and unsaturated boundary layer. Therefore, we refer to it as the boundary layer entropy (BLE) term for consistency with Emanuel (1994) and Agard (2017). It can be seen from (1) that increasing BLE increases SBCAPE. For an unsaturated boundary layer, and neglecting the effects of water vapor on the potential temperature and specific heat, we can write this term as

$$(T_i - T_{\mathrm{EL}})\frac{ds_i}{dt} = (T_i - T_{\mathrm{EL}})\frac{c_p}{\theta_e}\frac{d\theta_e}{dt}. \tag{2}$$

This equation was derived using the relationship between entropy and potential temperature (e.g., Emanuel 1994; Bryan 2008). The heating rate of the boundary layer $d\theta_e/dt$ is in general a combination of diabatic heating and advection, depending on the frame of reference of the parcel being lifted. Agard (2017) analyzed (1) in a Lagrangian frame, tracking boundary layer parcels as they were advected along by the low-level flow, and therefore the only sources for (2) were diabatic (since entropy is conserved following the motion for adiabatic flow). In our analysis, the parcel source is fixed relative to the ground, so advection of entropy into the boundary layer column must be explicitly accounted for when evaluating (2). We computed the time derivative $d\theta_e/dt$ using a simple second-order centered finite difference approximation with $\Delta t = 5$ min, and additionally expanded the derivative to explicitly compute the advective and diabatic terms (see section 4b).

Term B of (1) is the free-troposphere radiative heating term and is integrated from the LFC to the EL, i.e., only over the layer of positive parcel buoyancy (Emanuel 1994). It can be seen from Eq. (1) that radiative cooling of the cloud layer, or the free troposphere, increases SBCAPE, while warming decreases SBCAPE. Term C in (1), the relative advection (both

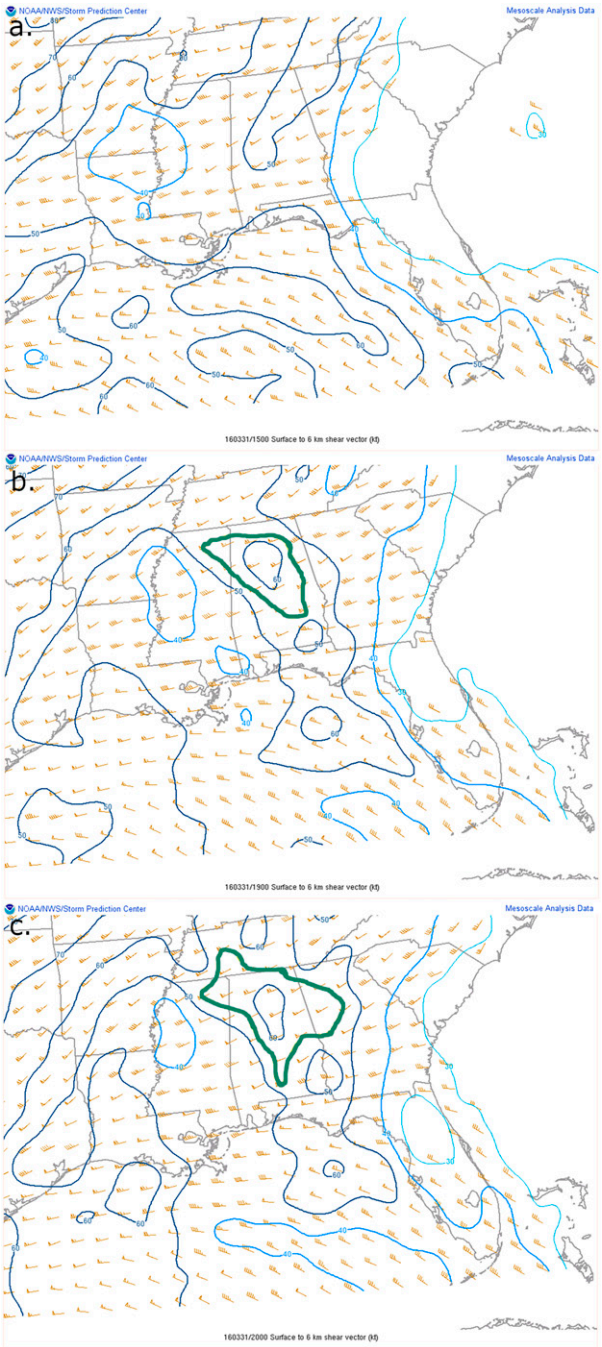

FIG. 5. Operational mesoanalysis (from the NWS Storm Prediction Center; Hart et al. 2014) of surface-to-6 km AGL shear vectors (kt) at (a) 1500, (b) 1900, and (c) 2000 UTC 31 Mar 2016. Pennants correspond to 50 kt, full barbs correspond to 10 kt, and half-barbs correspond to 5 kt. Contours are drawn every 10 kt, starting from 30 kt. The green annotations encompass the region of interest where shear values are above 55 kt.

Brought to you by NOAA Central Library | Unauthenticated | Downloaded 08/02/23 01:52 PM UTC

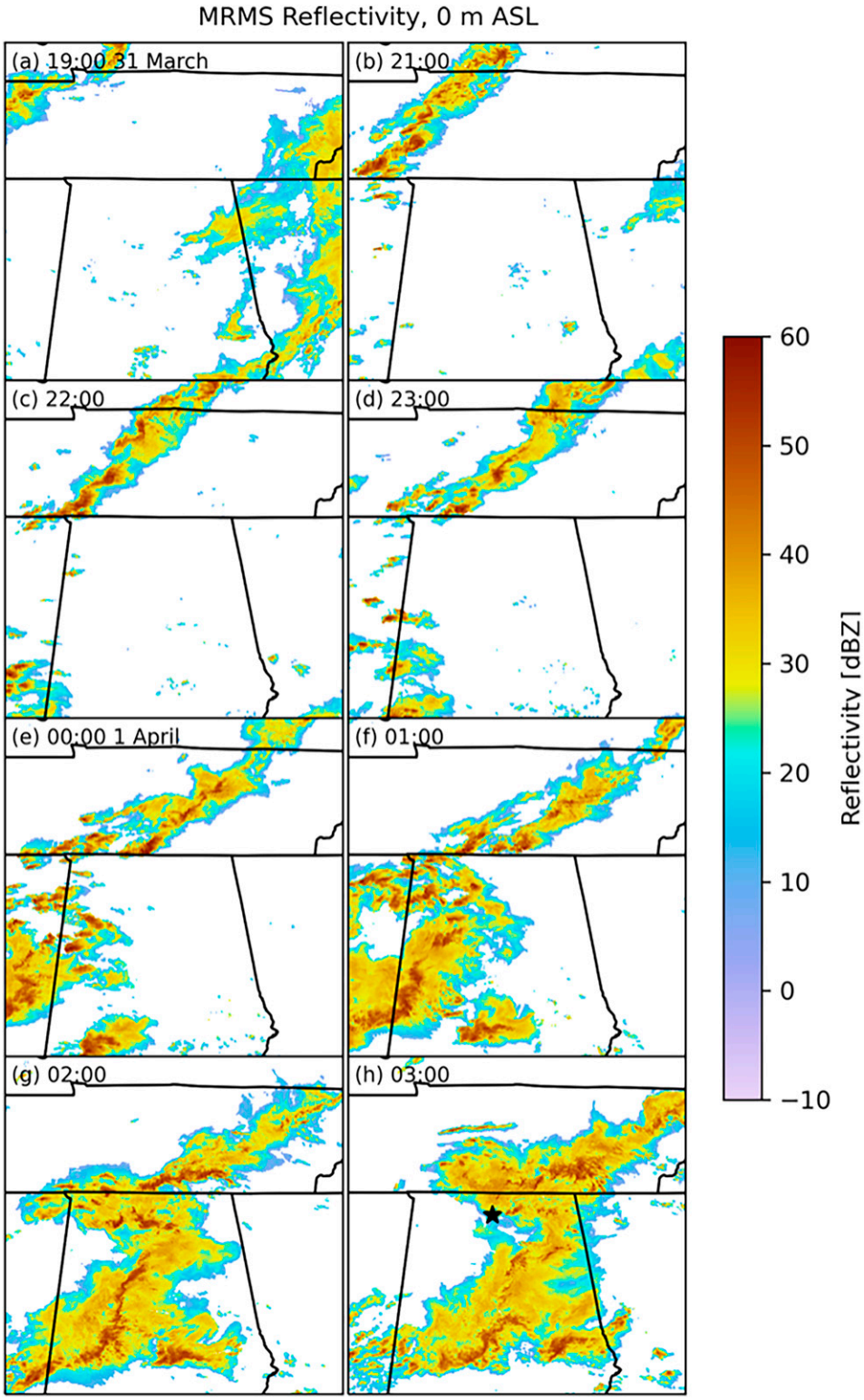

FIG. 6. MRMS reflectivity (dBZ) mosaic at 0 m MSL at (a) 1900, (b) 2100, (c) 2200, and (d) 2300 UTC 31 Mar 2016; and (e) 0000, (f) 0100, (g) 0200, and (h) 0300 UTC 1 Apr 2016. The black star in the center of (h) is the location of Belle Mina, AL. Radar image created using Py-ART (Helmus and Collis 2016).

Brought to you by NOAA Central Library | Unauthenticated | Downloaded 08/02/23 01:52 PM UTC

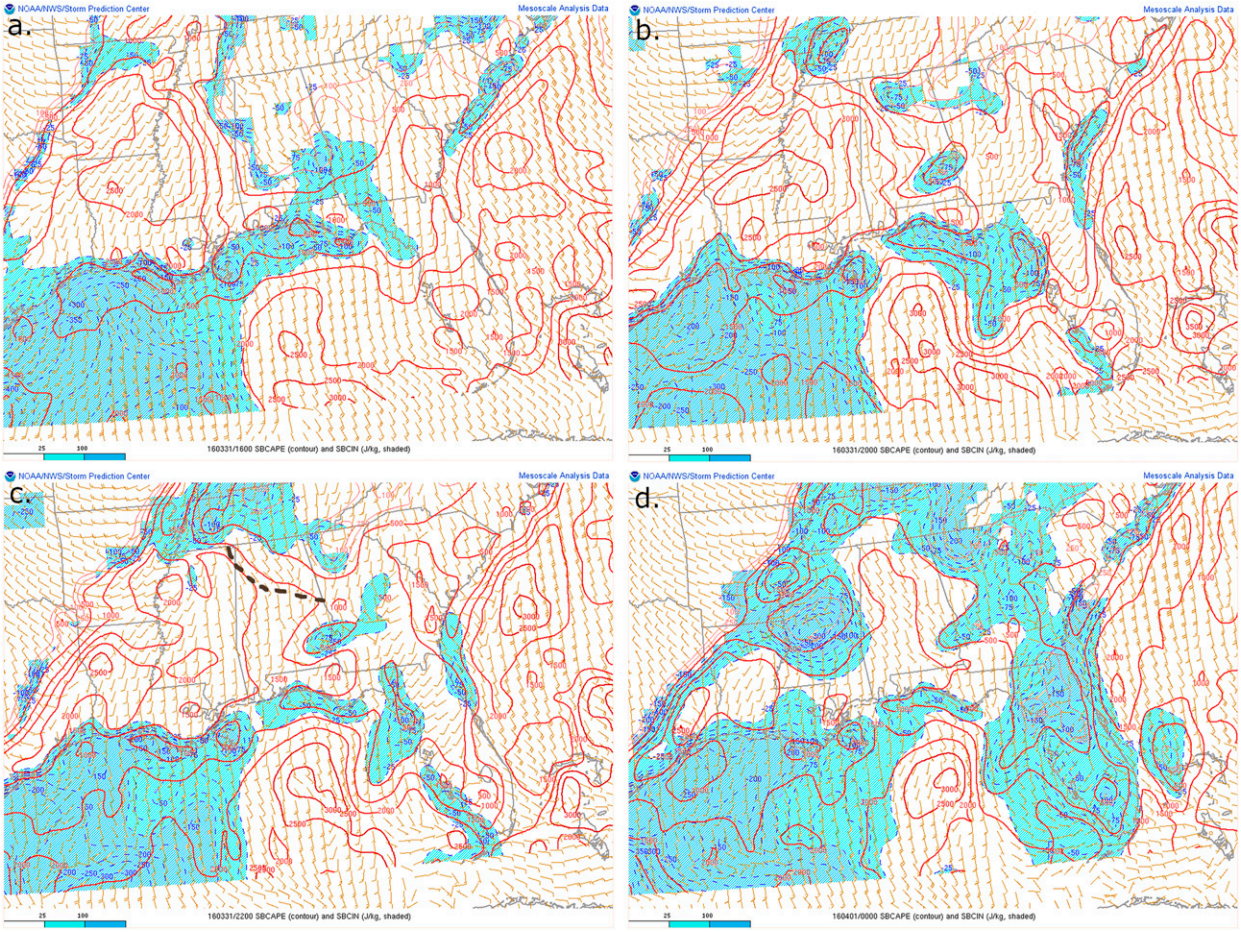

FIG. 7. Operational mesoscale analysis (from the NWS Storm Prediction Center) of SBCAPE and SBCIN (J kg^{-1}) over the SE United States at (a) 1600 UTC, just after the morning rain ended; (b) 2000 UTC, showing a relative minimum in CAPE over northern Alabama; and the recovery of CAPE from (c) 2200 UTC 31 Mar 2016 to (d) 0000 UTC 1 Apr 2016. SBCAPE is contoured in red every 500 J kg^{-1}, and SBCIN is contoured in blue every 50 J kg^{-1}. Surface winds are depicted as beige barbs; full barbs correspond to 10 kt, and half-barbs correspond to 5 kt. The brown annotation in (c) is an outflow boundary analyzed by the SPC.

horizontal, C1, and vertical, C2) term, is computed using a second-order centered spatial finite difference approximation and is also integrated from the LFC to the EL. Term C represents the effects of temperature advection in the free troposphere on SBCAPE; cooling this layer will increase the environmental lapse rate, which in turn will increase SBCAPE.

It is important to note that the direct effects of deep convection in the column are not accounted for in (1). The time frame over which we analyzed CAPE tendency was largely free of deep convection over the Belle Mina site in both the observations and model simulations until near the end of the period (~0100 UTC). However, the effects of deep convection upstream of the Belle Mina site may potentially be captured by the advective part of Term A as well as the free-tropospheric relative advection term (Term C).

Results from Agard (2017) and Agard and Emanuel (2017) found that Term A is likely to be dominant, and changes in the boundary layer (also can be referred to as subcloud layer), such as increases in temperature, will likely contribute most to changes in SBCAPE. In other words, their work suggests that boundary layer diabatic heating through solar insolation and associated fluxes of heat and moisture is the primary driver of SBCAPE buildup in many severe storm environments (Agard 2017; Agard and Emanuel 2017). This study is testing the applicability of this equation to our case by evaluating (1) on model output and comparing with a synthesis of conventionally available and special VORTEX-SE observations.

3. Case overview

a. *Description of VORTEX-SE IOP on 31 March 2016*

On 31 March 2016, a VORTEX-SE IOP (the third of 2016; hereafter IOP3) was declared in anticipation of convective storms in the domain. Nonsevere morning convection was expected in association with weak low-level (~0–3 km) CAPE, but in the afternoon the environment was expected to support stronger convection, including supercells, owing to rapid destabilization and moderate low-level wind shear (NWS Storm

Brought to you by NOAA Central Library | Unauthenticated | Downloaded 08/02/23 01:52 PM UTC

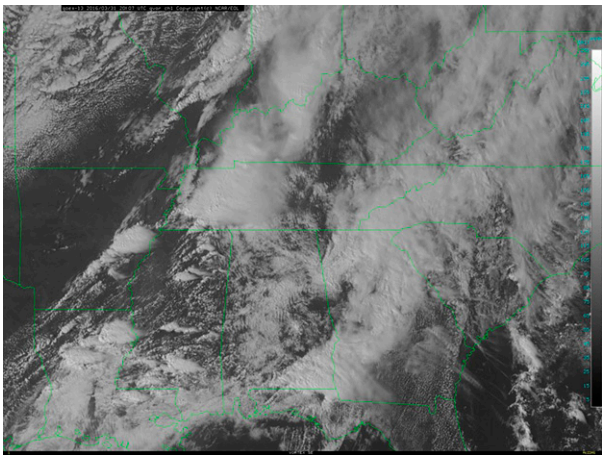

FIG. 8. The 1-km visible satellite imagery at 2207 UTC 31 Mar 2016. Image courtesy of NCAR.

Prediction Center 2016a; Rasmussen et al. 2015). The focus of VORTEX-SE field observations during the preconvective period of IOP3 was the rapid northward advection of warm, humid near-surface air as a morning convective system departed. Examining the conceptual model that moisture advection is the primary driver of destabilization in the SE United States was one objective of this work.

Figure 3 provides context of the upper-level winds, temperatures, and humidity for the region before the morning storms (12 UTC 31 March) and during the evening convection (01 UTC 1 April 2016). At 1200 UTC 31 March, a positively tilted, upper-level trough extended from central Alberta in Canada southwestward toward the four corners (Fig. 3a). An attendant subtropical jet streak, stretching from the Baja peninsula of Mexico to western Mississippi at 1200 UTC, rounded the base of this trough such that its right exit region was situated over northern Alabama (the VORTEX-SE domain) by 0000 UTC 1 April (Fig. 3b). While the trough progressed sluggishly eastward from 1200 UTC 31 March to 0000 UTC 1 April, its progress was sufficient to amplify the upper-level geopotential height gradient between the trough to the west and the mid-Atlantic ridge to the east, increasing the maximum winds in the subtropical jet streak (Fig. 3b). This, in turn, amplified upper-level flow and deep-layer shear over the VORTEX-SE domain (Fig. 3b). At the surface, a low pressure system remained nearly stationary over lower Michigan with a cold front extending southwestward through Texas (Figs. 3c,d). Like its attendant upper-level trough, this surface cold front progressed slowly eastward through the day, reaching the Mississippi River by 0000 UTC 1 April. It follows that this front was not the primary source of environmental heterogeneity over the VORTEX-SE domain in northern Alabama. East of the front, across nearly all of Alabama, southerly flow advected near-surface moisture northward from the Gulf of Mexico (Figs. 3c,d).

Widespread nonsevere storms did indeed move through the VORTEX-SE domain early in the morning on 31 March (Fig. 4). These storms were part of a remnant mesoscale convective system that moved eastward through Alabama and Tennessee the previous night. This morning rain and its associated cool outflow stabilized the boundary layer over northern Alabama. Owing to predicted destabilization over the VORTEX-SE domain and increasing deep-layer wind shear, an intensive observing period (IOP; Rasmussen and Koch 2016) was declared for the afternoon and evening of 31 March 2016.

Between 1500 and 2000 UTC, the 0–6-km shear over northern Alabama increased from westerly at ~40–55 kt (1 kt ≈ 0.51 m s^{-1}) to west-southwesterly at ~60–70 kt as depicted in Fig. 5. At 1900 UTC, thunderstorms developed over north central Mississippi (Fig. 6a). These afternoon storms were more discrete in nature when compared to the morning convection. The difference in the structure of the morning and afternoon convection is believed to be due to an absence of low-level CAPE for the morning convection (Rasmussen et al. 2015). These storms moved rapidly to the northeast (Fig. 6b), with some exhibiting weak rotation (not shown). Between 1900 and 2000 UTC the 0–6-km shear suggested possible heterogeneities in the environment in northern Alabama, as evident in the green contour on Figs. 5b and 5c. This area, which encloses shear values greater than 55 kt, grew from 1900 to 2000 UTC.

After 2100 UTC, the storms moved into air that was too stable to support low-level rotation (NWS Storm Prediction Center 2016b). The morning convection left a large-scale outflow boundary (Fig. 7c) extending from northern Mississippi to central Alabama, in an area which later exhibited strong speed shear at and above 2 km AGL, 0–1-km SRH around 200 m^2 s^{-2} (NWS Storm Prediction Center 2016a), and 0–6-km shear of 50–60 kt.

By 2200 UTC, storms with persistent low-level rotation (velocity not shown) had reached the Alabama–Tennessee border (Figs. 6c and 8), despite near-surface conditions being relatively cool and stable (Fig. 7c). At 2300 UTC, the NWS SPC issued a tornado watch covering northern Alabama and southern middle Tennessee, citing the potential for "supercells capable of hail, locally damaging winds, and tornadoes … to develop and move eastward to east-northeastward across the area overnight" (NWS Storm Prediction Center 2016e). Two areas on the Alabama–Mississippi and Alabama–Georgia borders, respectively, had developed a mix of discrete supercells and multicell clusters (Figs. 6d–f), supporting a tornado risk across northern Alabama (NWS Storm Prediction Center 2016c,d).

At 0000 UTC 1 April, the VORTEX-SE domain environment was characterized by backing and strengthening winds above 1 km AGL, 0–1 km AGL storm relative helicity (SRH) of 250 to 300 m^2 s^{-2}, and SBCAPE around 500 J kg^{-1} in Belle Mina and surrounding areas (Fig. 7d). Low-level warm air advection was also present closer to the Alabama–Georgia border (NWS Storm Prediction Center 2016c,d).

Over the next few hours, the northern storms (Figs. 6d–f) continued to exhibit low-level rotation (not shown). These storms moved over the VORTEX-SE domain, and one generated a tornado near Priceville, AL, approximately 22 km south of Belle Mina, at 0200 UTC (Fig. 6g). The tornado was rated an EF2 on the enhanced Fujita scale with maximum winds of 51.4 m s^{-1}. Its damage track was approximately 14 km long and 180 m wide (National Weather Service 2016). VORTEX-SE

Brought to you by NOAA Central Library | Unauthenticated | Downloaded 08/02/23 01:52 PM UTC

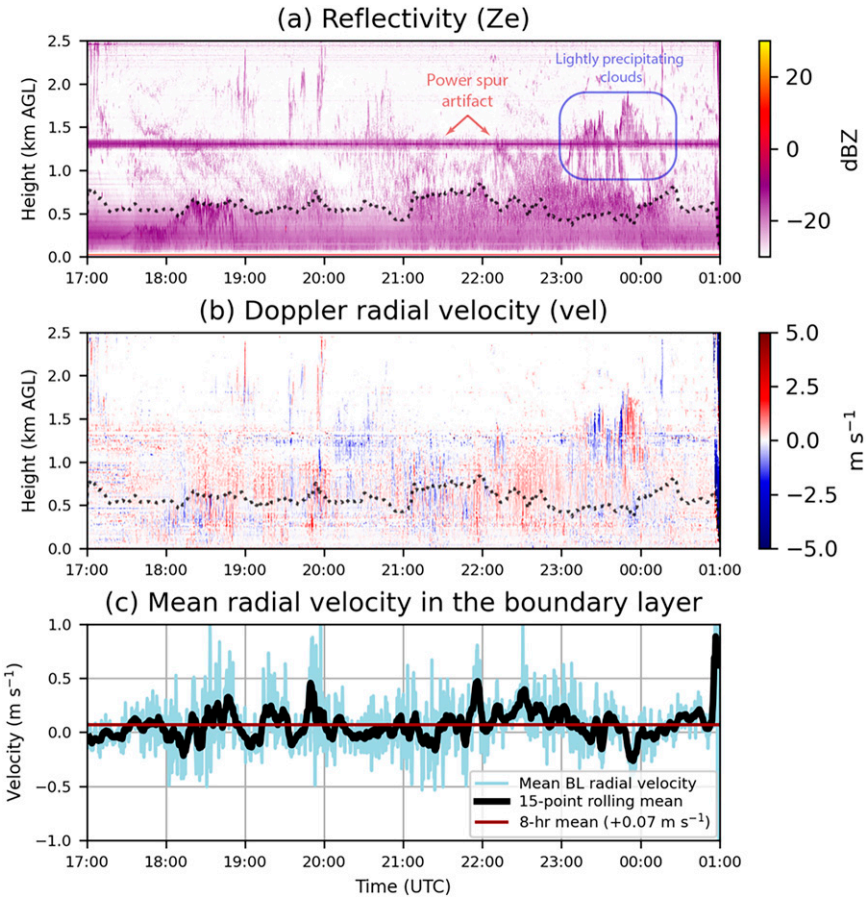

FIG. 9. Observations of (a) reflectivity (dBZ) and (b) Doppler velocity (m s^{-1}) by the vertically pointing UMass FMCW radar at Belle Mina, AL, from 1700 UTC 31 Mar 2016 to 0100 UTC 1 Apr 2016. In both (a) and (b), a dashed gray line follows an automatically detected boundary layer height (Lange et al. 2014, 2015). The reflectivity maximum appearing at 1.3 km AGL, and associated velocity discontinuities, are artifacts of power spurs in the UMass FMCW transmitter (Tanamachi et al. 2019). (c) Mean boundary layer vertical velocity (m s^{-1}) as a function of time (light blue line), with a 15-point rolling mean applied (heavy black line), and the overall mean for the plotted 8-h period (red horizonal line at +0.07 m s^{-1}).

IOP3 field observations ceased at 0300 UTC, when the storms exited the Huntsville domain (Fig. 6h).

b. Boundary layer development

The vertically pointing, UMass, S-band, FMCW radar (İnce et al. 2003) located in Belle Mina, AL (34.6568°N, 86.8792°W), observed high reflectivity in the morning precipitation, followed by refractive index turbulence (Bragg scatter) in the hydrometeor-free period that followed (Fig. 9a). After the cessation of rainfall at Belle Mina around 1650 UTC, the convective boundary layer (CBL) began to redevelop, reaching a depth of about 500 m by 1740 UTC (Fig. 9a). The boundary layer height then fluctuated between 500 and 750 m until 2100 UTC and remained above 750 m thereafter (Fig. 9a). The exception to that is between 2300 and 0000 UTC where the boundary layer height was closer to 500 m again when lightly precipitating clouds were present (Fig. 9a). While vertical velocity in the CBL (Fig. 9b) fluctuated in intensity and sign (Fig. 9c), indicating the unsteadiness of CBL thermal plumes, the overall mean vertical velocity was weakly positive (+0.07 m s^{-1}) over the hydrometeor-free period (1700 UTC 31 March–0100 UTC 1 April).

The boundary layer height time series depicted in Fig. 9a was objectively calculated using an extended Kalman filter (EKF)-based method (Lange et al. 2014, 2015). This algorithm iteratively fits an error function (erf) to the vertical profile of reflectivity, returning the boundary layer height as the function's inflection point and recalculating the error covariance matrix at each time step. This approach assumes that Bragg scatter (and hence reflectivity) will be maximized at or near the top of the precipitation-free boundary layer, before decreasing in the relatively scatterer-free troposphere (Lange et al. 2014). One weakness of this EKF-based approach is that erf-like reflectivity profiles can also be produced by phenomena other than Bragg scatter, such as clouds and precipitation.

Brought to you by NOAA Central Library | Unauthenticated | Downloaded 08/02/23 01:52 PM UTC

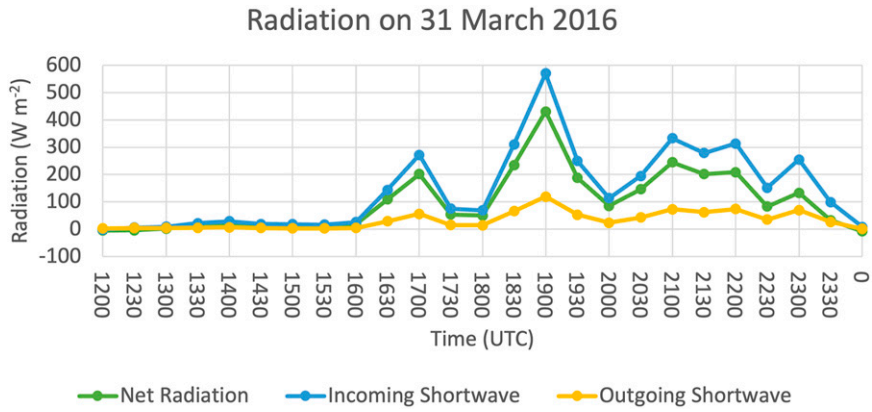

FIG. 10. Shortwave radiation data from a 2.5 m AGL meteorological tower at Belle Mina, AL. Data from Lee et al. (2016a). For reference, sunrise was at 1135 UTC 31 Mar and sunset was at 0008 UTC 1 Apr.

Layer misattribution error (Araújo da Silva et al. 2022) may cause the EKF method to give erroneous results when multiple scatterer layers are present. In the present case, however, the EKF method follows the top of the CBL accurately from 1800 to 2230 UTC (Fig. 9a), under clear sky conditions. After 2300 UTC, a lightly precipitating cloud layer developed between 1.0 and 1.5 km AGL (blue box in Fig. 9a). This cloud layer complicated CBL identification by intermittently suppressing convection, yielding CBL top heights that are likely to be underestimates of the true boundary layer depth from 2230 to 0100 UTC (Fig. 9a). Similar results were obtained by Araújo da Silva et al. (2022) on cloudy days during an observation campaign in Germany. However, during the period under discussion, the objectively identified boundary layer top remained below the cloud layer, indicating that the algorithm avoided misidentifying the cloud layer (as well as an artificial reflectivity maximum at 1.3 km AGL; Tanamachi et al. 2019) as the top of the CBL.

4. Results: Analysis of CAPE development

a. *Observed and modeled SBCAPE development*

Following the morning rain on 31 March, the SBCAPE at Belle Mina increased from near zero to over 500 J kg^{-1} between 2000 and 2200 UTC according to the observed ATDD

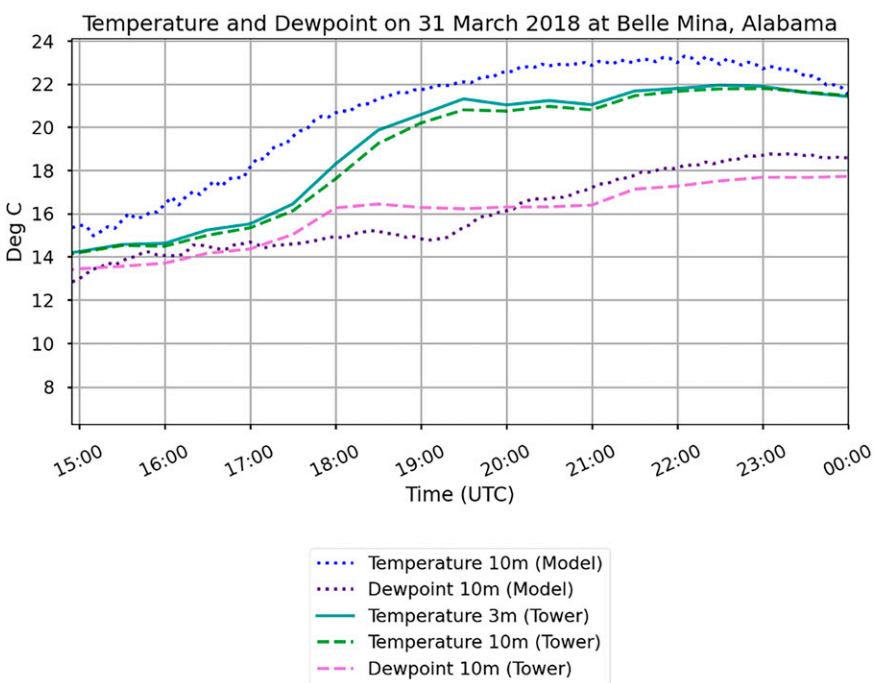

FIG. 11. Temperature (°C) at 3 and 10 m AGL and dewpoint at 10 m from the meteorological tower at Belle Mina, AL (Lee et al. 2016a), and temperature and dewpoint at 10 m from the ARPS model at the grid point closest to Belle Mina, AL.

Brought to you by NOAA Central Library | Unauthenticated | Downloaded 08/02/23 01:52 PM UTC

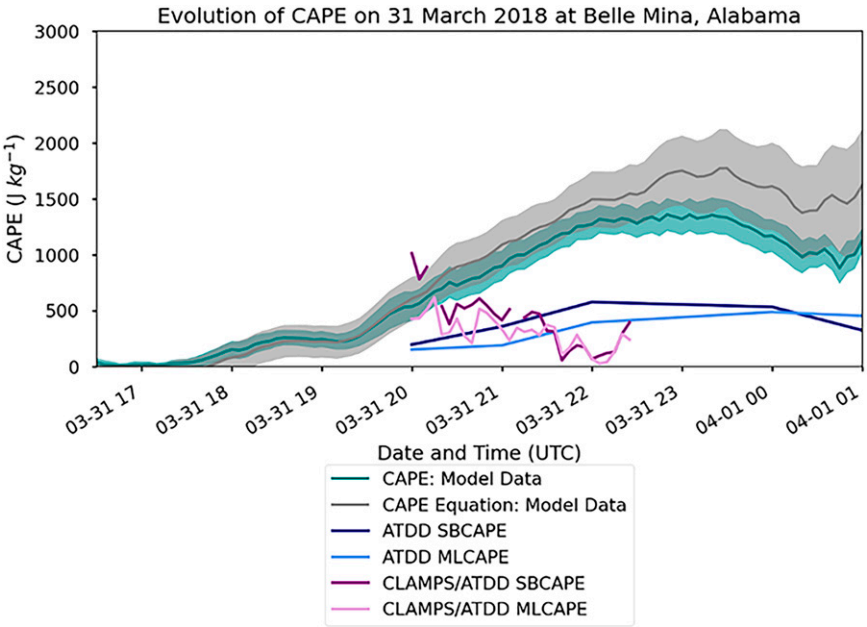

FIG. 12. ML CAPE values (J kg^{-1}) calculated from the ARPS ensemble mean (blue), ATDD soundings (gray), constructed ATDD/CLAMPS soundings (purple), and the model ensemble mean integrated CAPE tendency equation (green) from 2000 UTC 31 Mar 2016 to 0200 UTC 1 Apr 2016. The shaded areas are the standard deviation of the values.

soundings. During that time, shortwave solar insolation (measured by the ATDD instrumented tower) increased over the Belle Mina site (Fig. 10), contributing to surface heating over the area (Fig. 11). The increased near-surface air temperatures contributed to the increase in SBCAPE.

While hourly soundings are useful, they are still too coarse temporally to resolve rapid changes in CAPE. To estimate subhourly CAPE changes, the CLAMPS temperature and moisture profiles, which extended from the surface to 4 km AGL, were combined with temporally interpolated ATDD soundings above 4 km AGL to create constructed soundings every five minutes from 2000 to 2200 UTC 31 March. The linear temporal interpolation between the hourly ATDD soundings was done to match the temporal resolution of the CLAMPS data, and to avoid large discontinuities in CAPE resulting from sudden changes in the profile above 4 km AGL. The results of this interpolation are shown in Fig. 12 (purple line). From these constructed soundings, CAPE and other parameters were calculated at 5-min intervals over the period. It was found that MLCAPE was initially 400 J kg^{-1} and peaked at about 750 J kg^{-1} at 2015 UTC (Fig. 12). SBCAPE started out around 1000 J kg^{-1} and fell to around 500 J kg after 2030 UTC. After that time CAPE hovered around the MLCAPE values. The only exception to this is at two-time steps where SBCAPE fell to 0 J kg^{-1} (gaps in dark purple line; likely due to a known issue in the Metpy calculation routine). Since MLCAPE is calculated over a deeper layer, it is less sensitive to changes in surface temperature and dewpoint than SBCAPE.

We also calculated SBCAPE from the model grid column closest to the Belle Mina site (Fig. 12, green) and compared this with the SBCAPE computed from integrating the CAPE tendency equation (Fig. 12, blue). This comparison was done to quantify how well the SBCAPE integrated from the SBCAPE tendency equation agreed with that computed directly from the model profiles. The two are in reasonable agreement; discrepancies arise from a combination of discretization error and the effects of data assimilation. In more detail surface observations were assimilated every 15 min, so any errors in the EnKF analysis may have cumulative effects independent from the forward model. The maximum SBCAPE calculated from the model ensemble mean during the late afternoon was ~1400 J kg^{-1}, which is substantially larger than that computed from the ATDD soundings and the hybrid ATDD/CLAMPS-constructed soundings. The lower SBCAPE values in the hybrid soundings resulted from greater low-level moisture in the ATDD soundings than in the CLAMPS-derived soundings. The SBCAPE computed directly from the model and from integrating (1) using model data both rise steadily until about 2000 UTC, after which they remain relatively constant until ~2300 UTC. Then, after 2300 UTC, the model derived SBCAPE decreases slowly and at roughly the same rate as that computed from the ATDD soundings until ~0030 UTC. Overall, the model predicted higher SBCAPE peaking later than the observations. This is at least partially explained by the fact that the model predicted surface temperatures were consistently ~2 K higher than the observations (Fig. 11). Another experiment was performed on the 3-km grid in which radar data were withheld from the assimilation; this experiment resulted in lower SBCAPE closer to that of the observations and peaking at around the same time (not shown), although with much greater spread across the ensemble. This experiment also produced a large amount of spurious convection over northern

Brought to you by NOAA Central Library | Unauthenticated | Downloaded 08/02/23 01:52 PM UTC

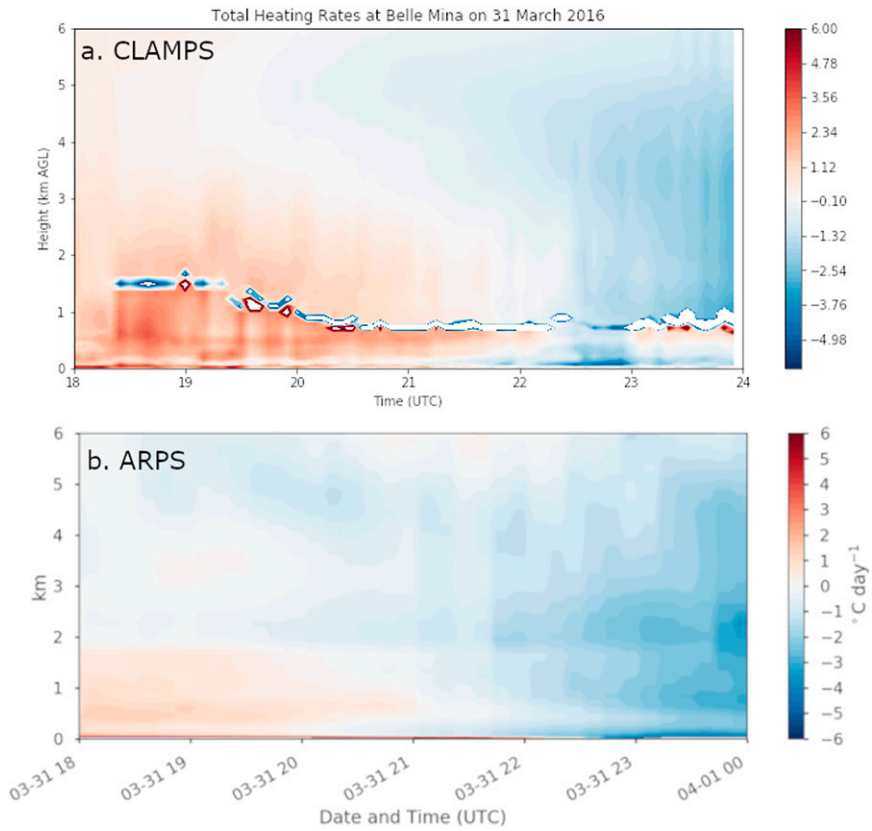

FIG. 13. The total (longwave plus shortwave) radiative heating rate (K day^{-1}) computed from the (a) CLAMPS observations using the RRTM on 31 Mar 2016 and (b) ARPS model. The thin layer of larger radiative cooling with a lot of noise in (a) is associated with the radiative cooling at the top of the thin stratiform cloud layer.

Alabama during the mid-to-late afternoon (not shown) and was thus not analyzed further.

To better understand the role of both boundary layer and free-troposphere radiative heating/cooling, we calculated the vertical profile of the total radiative heating rate over the Belle Mina site from the CLAMPS observations using the longwave and shortwave versions of the Rapid Radiative Transfer Model (RRTM; Mlawer et al. 1997; Clough et al. 2005). We then compared the time evolution of these radiative heating rates directly with the radiative heating profile from the ARPS ensemble mean interpolated to the Belle Mina location (Fig. 13). The BL radiatively warmed until about 2200 UTC (driven primarily by shortwave absorption), then radiatively cooled for about an hour when the clouds were optically thin (i.e., had liquid water paths smaller than about 20 g m^{-2}), and then began to warm again below the optically thicker clouds at about 2300 UTC (Fig. 13a). The radiative heating rate from the ARPS model agreed qualitatively with the RRTM calculations using the CLAMPS observations (Fig. 13b) below the cloud layer, especially between 1800 and 2100 UTC, with a general cooling trend in both the model and observations. Otherwise, the CLAMPS exhibits a somewhat deeper layer of heating above the cloud layer than the ARPS, especially early in the period. Some of this discrepancy may be due to the relatively coarse resolution of the AERI profiles above the boundary layer.

b. *Time tendency/components of SBCAPE*

The ARPS simulations produced southerly winds (not shown) and increasing θ_e over northern Alabama over the course of the afternoon (Figs. 14a–c), consistent with heating and moistening of the boundary layer via advection or surface fluxes or a combination of the two. In both the simulations (Fig. 15) and observations from CLAMPS (Fig. 16), low-level temperature and moisture (below 500 m AGL) at the Belle Mina site increased steadily from midmorning (~1500 UTC) to late evening (0000 UTC). This heating coincides with increased incoming solar (shortwave) radiation (Fig. 10). Additionally, the increase in the moisture at low levels in the ARPS at 1800 UTC agrees with the AERI retrievals (Figs. 15 and 16); however, the AERI shows that the second increase of moisture comes at ~2100 UTC whereas the ARPS has that second increase occurring somewhat earlier (~2000 UTC).

To examine the contributions to SBCAPE in more detail, we evaluated each of the terms of the time tendency of SBCAPE [Eq. (1)] using the model output, for each fifteen-minute interval from 1200 UTC 31 March to 0200 UTC 1 April (Fig. 17). Prior to ~1745 UTC, the modeled SBCAPE was 0 J kg^{-1}, as

Brought to you by NOAA Central Library | Unauthenticated | Downloaded 08/02/23 01:52 PM UTC

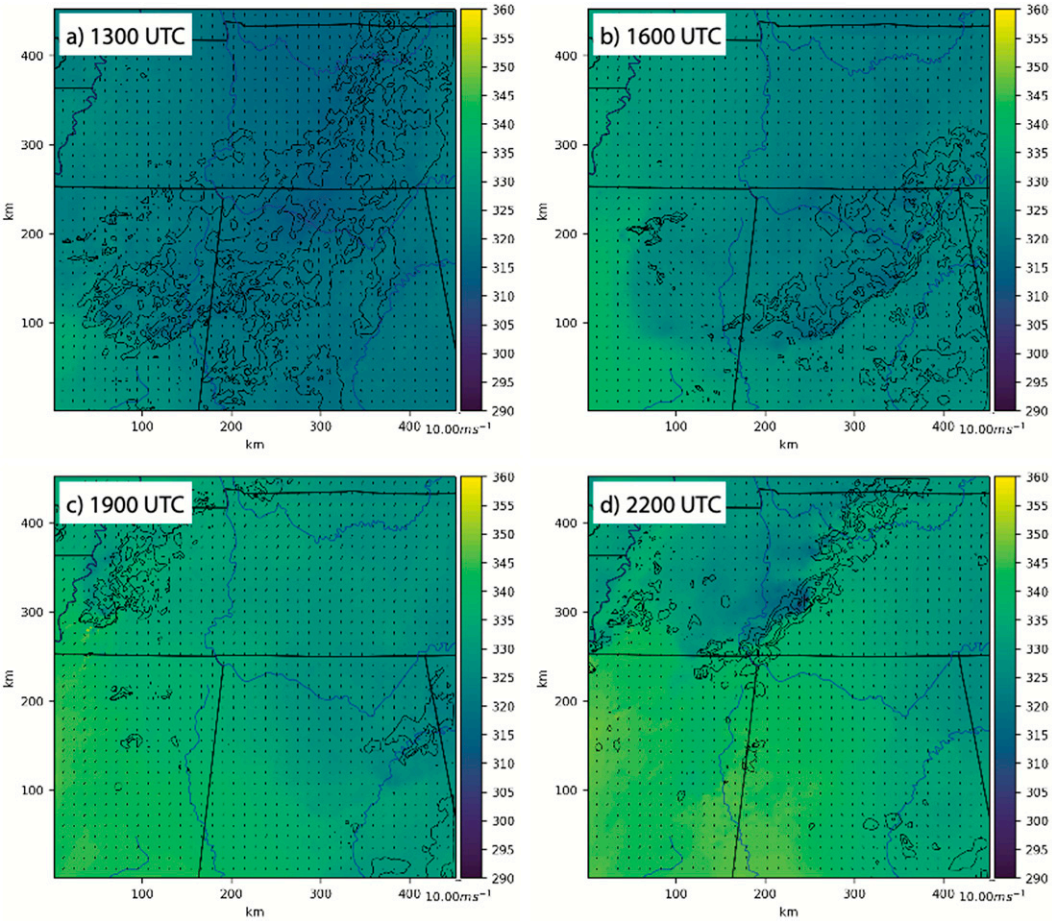

FIG. 14. ARPS ensemble mean surface θ_e (color fill; K) and radar reflectivity (dBZ; black contours, 10-dBZ increment, starting at 30 dBZ) on the 3-km domain at (a) 1300, (b) 1600, (c) 1900, and (d) 2200 UTC.

were all the components of the SBCAPE tendency. SBCAPE calculated from the reconstructed ATDD/CLAMPS soundings reached its peak after 2015 UTC, which was before the peak in the ATDD soundings (2200 UTC) and that in the ARPS model (~2300 UTC) (Fig. 12). We hypothesize a subsidence inversion between 800 and 900 hPa (Figs. 1b,c) played a role in reducing the observed SBCAPE. This inversion was not captured in the model and may have contributed to the higher model derived SBCAPE over the event.

An analysis of the individual integrated terms of the SBCAPE tendency equation across the ARPS ensemble (Fig. 17) demonstrates that the greatest positive contributor to SBCAPE was BLE tendency [i.e., Term A in Eq. (1)]. In the mean, the free-tropospheric vertical advection term (C2) contributed weakly to decreasing SBCAPE especially after 2100 UTC. In contrast, the free-tropospheric horizontal advection term (C1) contributed weakly negatively prior to ~2100 UTC and then increasingly positively (in the mean) to SBCAPE thereafter. The contributions from terms C1 and C2 tended to compensate for each other. While the contribution of CAPE from C1 was not as relevant for our study, it could be a contributor to destabilization after dark in the SE United States, as explored by King et al. (2017). They found that low-level positive θ_e advection was the primary reason surface temperatures increased in their simulations of various HSLC environments. Along with the surface warming, they also found that cooling aloft (due to several mechanisms including both horizontal cold air advection and lift) also contributed to destabilization of the environment in many cases. (King et al. 2017).

The contribution from the free-tropospheric radiative heating term (Term B) was negligible throughout the period. The ensemble spread tended to increase somewhat after ~0000 UTC for each term except the radiative heating term. The increased spread appears to be a result of deep convection overspreading the Belle Mina site (not shown) that varies substantially in its intensity and specific timing—and therefore its effects on the model state variables that constitute the terms in (1)—across the ensemble during this period. As mentioned previously, the CAPE tendency equation (1) does not account for the effects of deep convection; the increase in ensemble spread is a helpful indicator of the loss of reliability after 0000 UTC. Additionally, in the observed soundings it is evident subsidence is influencing the region; however, the model did not capture this subsidence after 2000 UTC.

Brought to you by NOAA Central Library | Unauthenticated | Downloaded 08/02/23 01:52 PM UTC

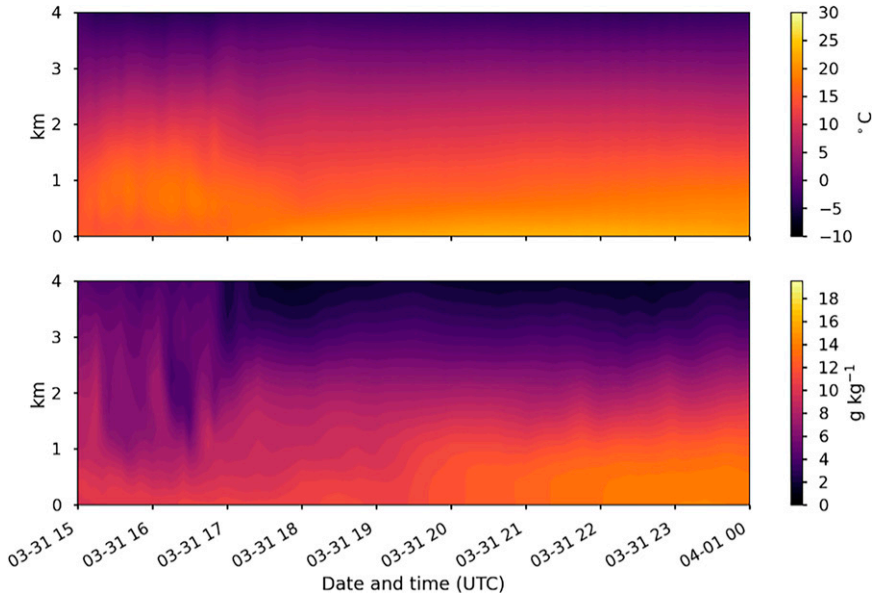

FIG. 15. Time–height plots of (top) temperature (°C) and (bottom) water vapor mixing ratio (g kg^{-1}) interpolated to the location of Belle Mina, AL, from the ARPS ensemble mean from 1500 UTC 31 Mar 2016 to 0000 UTC 1 Apr 2016.

Since the BLE term is the largest contributor to increasing SBCAPE, the question then arises as to what processes are most important to increasing BLE in this case. In general, BLE can increase through positive sensible and latent heat fluxes from the underlying surface, direct radiative heating, or advection into the fixed column. Expanding the temporal derivative in (2) yields the following equation for the SBCAPE tendency owing to BLE changes:

$$(T_i - T_{\mathrm{EL}})\frac{c_p}{\theta_e}\frac{\partial\theta_e}{\partial t} = (T_i - T_{\mathrm{EL}})\left[-\frac{c_p}{\theta_e}\mathbf{v}\cdot\nabla\theta_e + \frac{\dot{Q}}{T} + S\right], \quad (3)$$

where the three terms in square brackets represent the advection, radiative heating, and additional sources/sinks of entropy (denoted by S), respectively. The source term S primarily constitutes the near-surface flux divergence of sensible and latent heat, which are available as diagnostic output from the ARPS model. To determine the cause of the increase in boundary layer entropy, we calculated and integrated the terms in (3) from 5-min model output in a manner similar to that of the full CAPE tendency equation (1). The sum of the integrated terms on the RHS agrees qualitatively well with, but is somewhat larger than, the separate direct integral of the finite difference approximation to the local time derivative on the LHS of (3) (Fig. 18, purple and green bands, respectively). As in the case of the full SBCAPE tendency analysis, the discrepancy is likely due to a combination of discretization error and the effects of data assimilation.

Recall that the boundary layer has the highest radiative heating rates during the period of the highest SBCAPE increase (Fig. 13). The integral of the radiative heating term in (3) confirms that this term positively contributed to SBCAPE (Fig. 18, gray). However, by far the largest contribution to increasing SBCAPE from increasing BLE comes from the surface sensible and latent heat fluxes (Fig. 18, blue), in agreement with the results of Agard (2017). Advection also positively contributes to increasing SBCAPE (Fig. 18, red) to roughly the same degree as direct radiative heating. It should be noted that the direct radiative heating term in (3) is not the same as that in (1), the latter of which is computed in the free troposphere and integrated between the LFC and EL.

5. Conclusions

We conclude with high confidence that an increase in boundary layer entropy was the largest contributor to SBCAPE recovery at Belle Mina, AL, on 31 March 2016. Specifically, we are moderately confident that entropy increase due to surface heating was the primary source of SBCAPE increase, as supported by an analysis of the boundary layer entropy tendency equation (Fig. 18). This result agrees with those of Agard (2017) and stands somewhat in contrast with conventional wisdom suggesting that moisture advection should be the primary driver of destabilization close to the Gulf coast. We observed substantial variations in SBCAPE tendency on subhourly scales in both observations and numerical simulations (Fig. 12). This result underscores the need for frequent observations of the atmospheric boundary layer on days when severe weather is deemed likely. A system such as the CLAMPS can serve as a high temporal resolution substitute for radiosonde soundings in the boundary layer when soundings are not available. Optimally, several CLAMPS would be deployed in a network across the inflow region in advance of severe weather, so that temporal trends and the spatial pattern of CAPE and other stability parameters can be monitored in real-time. While the thermodynamic retrievals from the AERI in CLAMPS has some vertical resolution

Brought to you by NOAA Central Library | Unauthenticated | Downloaded 08/02/23 01:52 PM UTC

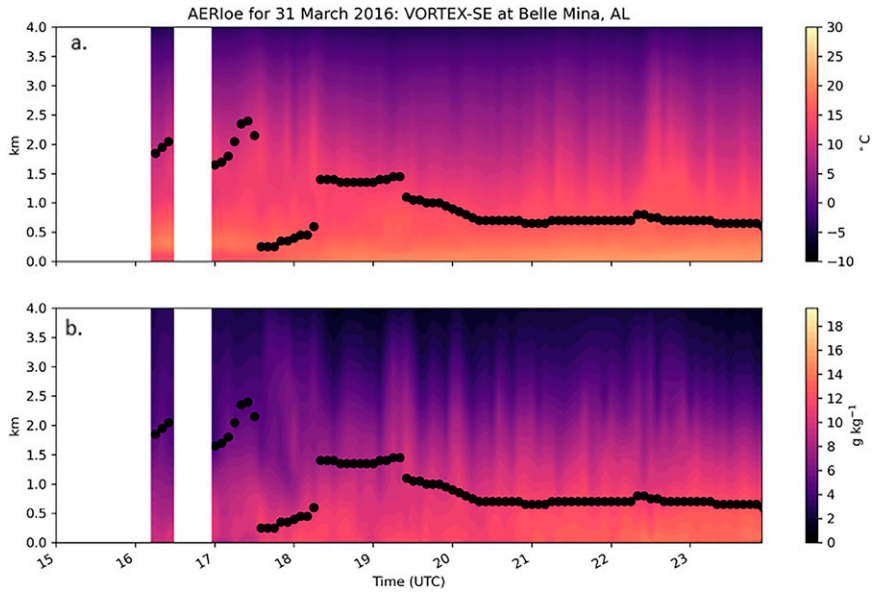

FIG. 16. Time–height plot of (a) temperature (°C) and (b) water vapor mixing ratio (g kg^{-1}) retrieved from the CLAMPS. The black dots represent cloud base heights. The vertical white areas indicate times when the AERI's hatch was closed due to precipitation, and thus no retrievals were possible.

limitations, Blumberg et al. (2017) showed that there is high correlation ($r > 0.9$) between radiosonde-observed and AERI-derived CAPE values.

Despite having supplemental VORTEX-SE observations over Belle Mina, our analysis is only valid at one point, and our methodology required numerical model fields to estimate the contribution of advection to CAPE recovery. During this IOP, additional soundings were launched at other sites in the VORTEX-SE domain, but these were primarily launched to the west of Belle Mina, whereas our primary interest was in boundary layer conditions south of Belle Mina, closer to the Gulf of Mexico moisture source. Additional soundings south

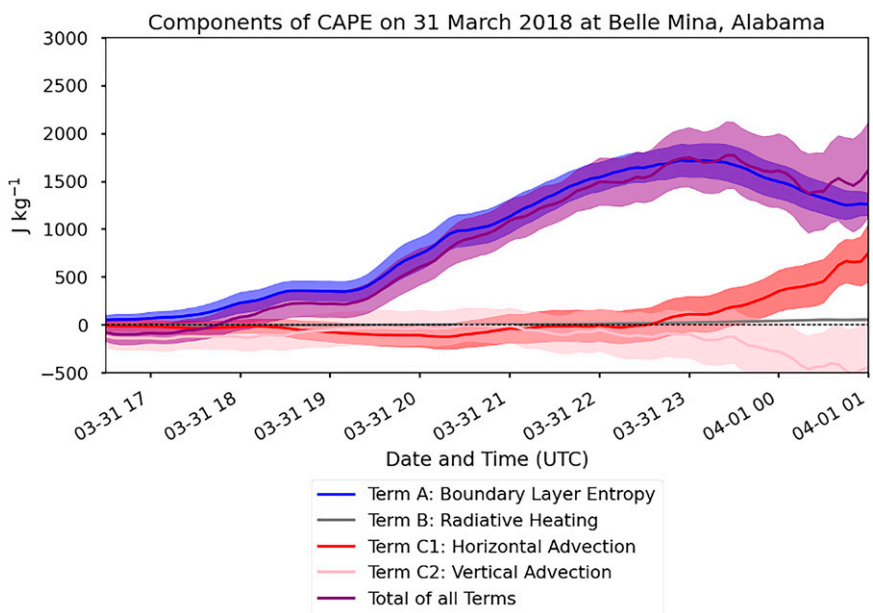

FIG. 17. Integrated contribution to CAPE (J kg^{-1}) of terms in the CAPE tendency equation (1), calculated from the ARPS simulations at the grid point closest to Belle Mina. The shaded areas encompass the standard deviation of the values.

Brought to you by NOAA Central Library | Unauthenticated | Downloaded 08/02/23 01:52 PM UTC

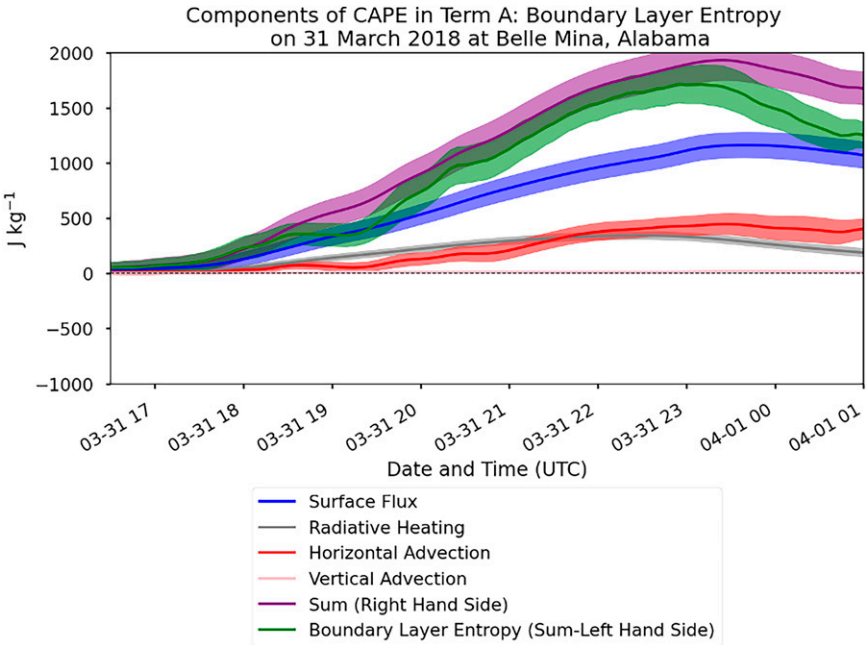

FIG. 18. As in Fig. 17, but for terms in the BLE tendency equation (3). The BLE (LHS) in green refers to the explicit time integral of the lhs of (3) and is identical to the BLE term plotted in Fig. 17. The shaded areas are the standard deviation of the values.

of the VORTEX-SE domain would have mitigated the need for numerical model estimates of advection, although these would still be coarse in temporal resolution. In short, current operational observations are not at a high enough temporal resolution for this analysis. Spatial resolution was not directly addressed in this study, because the field campaign design already addressed this issue to some extent. To better resolve these rapid, small-scale CAPE variations, surface and upper-air observations need to be collected subhourly and with sufficiently high spatial resolution (~5 km or less) for such small-scale influences to be characterized and their impacts on subsequent severe weather anticipated.

Acknowledgments. Collection and analysis of VORTEX-SE 2016 data were funded by National Oceanic and Atmospheric Administration Grant NA15OAR4590231. We gratefully acknowledge other VORTEX-SE participants for the sharing of their observations, particularly NOAA/ATD and NCAR/EOL for the Belle Mina sounding and radiation data. We also acknowledge Kevin Knupp and Tony Lyza for suggesting the Belle Mina deployment site for UMass FMCW and CLAMPS, and to Temple Lee and Bruce Baker for arranging land use permission, power, and internet connectivity with the Tennessee Valley Authority. We are indebted to Ming Xue, Youngsun Jung, Nathan Snook, Tim Supinie, and the rest of the team at the Center for Analysis and Prediction of Storms (CAPS) for providing the ARPS-EnKF code and assistance with running the system. Stephen Frasier and Joseph Waldinger (University of Massachusetts—Amherst) provided the UMass FMCW radar observations. We thank Sherman Fredrickson and Doug Kennedy for their help in deploying the CLAMPS at Belle Mina. We also acknowledge Connor Belak for his support in plotting the ARPS model data. The constructive comments of three anonymous reviewers greatly improved the manuscript. The statements, findings, conclusions, and recommendations are those of the authors and do not necessarily reflect the views of the NOAA or the U.S. Department of Commerce.

Data availability statement. Data from this project can be found on the VORTEX-SE NCAR EOL archive, found at https://data.eol.ucar.edu/master_lists/generated/vortex-se_2016/. The CLAMPS data can be found at doi:10.5065/D6154FFP as referenced in Turner (2016). The micrometeorological tower data and sounding data can be found at doi:10.5065/d6bg2mbj and doi:10.5065/d68k77fn respectively, as cited in Lee et al. (2016a,b). Birmingham sounding data and KTHX radar data are openly available from the National Center for Environmental Information (NCEI).

REFERENCES

Agard, J. V., 2017: Dependence of continental severe convective instability on climatological environmental conditions. Ph.D. dissertation, Massachusetts Institute of Technology, 119 pp.

——, and K. Emanuel, 2017: Clausius–Clapeyron scaling of peak CAPE in continental convective storm environments. *J. Atmos. Sci.*, **74**, 3043–3054, https://doi.org/10.1175/JAS-D-16-0352.1.

Anderson, J. L., 2001: An ensemble adjustment Kalman filter for data assimilation. *Mon. Wea. Rev.*, **129**, 2884–2903, https://doi.org/10.1175/1520-0493(2001)129<2884:AEAKFF>2.0.CO;2.

Brought to you by NOAA Central Library | Unauthenticated | Downloaded 08/02/23 01:52 PM UTC

Anderson-Frey, A. K., Y. P. Richardson, A. R. Dean, R. L. Thompson, and B. T. Smith, 2016: Investigation of near-storm environments for tornado events and warnings. *Wea. Forecasting*, **31**, 1771–1790, https://doi.org/10.1175/WAF-D-16-0046.1.

Araújo da Silva, M. P., F. Rocadenbosch, R. L. Tanamachi, and U. Saeed, 2022: Motivating a synergistic mixing-layer height retrieval method using backscatter lidar returns and microwave-radiometer temperature observations. *IEEE Trans. Geosci. Remote Sens.*, **60**, 1–18, https://doi.org/10.1109/TGRS.2022.3158401.

Ashley, W. S., 2007: Spatial and temporal analysis of tornado fatalities in the United States: 1880–2005. *Wea. Forecasting*, **22**, 1214–1228, https://doi.org/10.1175/2007WAF2007004.1.

Blumberg, W. G., D. D. Turner, U. Löhnert, and S. Castleberry, 2015: Ground-based temperature and humidity profiling using spectral infrared and microwave observations. Part II: Actual retrieval performance in clear-sky and cloudy conditions. *J. Appl. Meteor. Climatol.*, **54**, 2305–2319, https://doi.org/10.1175/JAMC-D-15-0005.1.

——, T. J. Wagner, D. D. Turner, and J. Correia Jr., 2017: Quantifying the accuracy and uncertainty of diurnal thermodynamic profiles and convection indices derived from the Atmospheric Emitted Radiance Interferometer. *J. Appl. Meteor. Climatol.*, **56**, 2747–2766, https://doi.org/10.1175/JAMC-D-17-0036.1.

Bryan, G. H., 2008: On the computation of pseudoadiabatic entropy and equivalent potential temperature. *Mon. Wea. Rev.*, **136**, 5239–5245, https://doi.org/10.1175/2008MWR2593.1.

Childs, S. J., R. S. Schumacher, and J. T. Allen, 2018: Cold-season tornadoes: Climatological and meteorological insights. *Wea. Forecasting*, **33**, 671–691, https://doi.org/10.1175/WAF-D-17-0120.1.

Chou, M.-D., 1990: Parameterization for the absorption of solar radiation by O_2 and CO_2 with application to climate studies. *J. Climate*, **3**, 209–217, https://doi.org/10.1175/1520-0442(1990)003<0209:PFTAOS>2.0.CO;2.

——, 1992: A solar radiation model for climate studies. *J. Atmos. Sci.*, **49**, 762–772, https://doi.org/10.1175/1520-0469(1992)049<0762:ASRMFU>2.0.CO;2.

——, and M. J. Suarez, 1994: An efficient thermal infrared radiation parameterization for use in general circulation models. NASA Tech Memo. 104606, 85 pp., https://archive.org/details/nasa_techdoc_19950009331.

Clough, S. A., M. W. Shephard, E. J. Mlawer, J. S. Delamere, M. J. Iacono, K. Cady-Pereira, S. Boukabara, and P. D. Brown, 2005: Atmospheric radiative transfer modeling: A summary of the AER codes. *J. Quant. Spectrosc. Radiat. Transfer*, **91**, 233–244, https://doi.org/10.1016/j.jqsrt.2004.05.058.

Dawson, D. T., II, L. J. Wicker, E. R. Mansell, Y. Jung, and M. Xue, 2013: Low-level polarimetric radar signatures in EnKF analyses and forecasts of the May 8, 2003 Oklahoma City tornadic supercell: Impact of multimoment microphysics and comparisons with observation. *Adv. Meteor.*, **2013**, 818394, https://doi.org/10.1155/2013/818394.

——, E. R. Mansell, Y. Jung, L. J. Wicker, M. R. Kumjian, and M. Xue, 2014: Low-level ZDR signatures in supercell forward flanks: The role of size sorting and melting of hail. *J. Atmos. Sci.*, **71**, 276–299, https://doi.org/10.1175/JAS-D-13-0118.1.

Doswell, C. A., III, and E. Rasmussen, 1994: The effect of neglecting the virtual temperature correction on CAPE calculations. *Wea. Forecasting*, **9**, 625–629, https://doi.org/10.1175/1520-0434(1994)009<0625:TEONTV>2.0.CO;2.

Emanuel, K. A., Ed., 1994: Deep convective regimes. *Atmospheric Convection*, Oxford University Press, 463–487.

Geerts, B., and Coauthors, 2017: The 2015 Plains Elevated Convection at Night field project. *Bull. Amer. Meteor. Soc.*, **98**, 767–786, https://doi.org/10.1175/BAMS-D-15-00257.1.

Hart, J., P. Marsh, and R. Thompson, 2016: SPC Mesoscale Analysis. NOAA/NWS Storm Prediction Center, accessed 25 January 2018, https://www.spc.noaa.gov/exper/mesoanalysis/.

Helmus, J. J., and S. M. Collis, 2016: The Python ARM radar toolkit (Py-ART), a library for working with weather radar data in the Python programming language. *J. Open Res. Software*, **4**, e25, https://doi.org/10.5334/jors.119.

İnce, T., S. J. Frasier, A. Muschinski, and A. L. Pazmany, 2003: An S-band frequency-modulated continuous-wave boundary layer profiler: Description and initial results. *Radio Sci.*, **38**, 1072, https://doi.org/10.1029/2002RS002753.

Janjić, Z. I., 2003: A nonhydrostatic model based on a new approach. *Meteor. Atmos. Phys.*, **82**, 271–285, https://doi.org/10.1007/s00703-001-0587-6.

Jung, Y., M. Xue, and M. Tong, 2012: Ensemble Kalman filter analyses of the 29–30 May 2004 Oklahoma tornadic thunderstorm using one- and two-moment bulk microphysics schemes, with verification against polarimetric radar data. *Mon. Wea. Rev.*, **140**, 1457–1475, https://doi.org/10.1175/MWR-D-11-00032.1.

King, J. R., M. D. Parker, K. D. Sherburn, and G. M. Lackmann, 2017: Rapid evolution of cool season, low-CAPE severe thunderstorm environments. *Wea. Forecasting*, **32**, 763–779, https://doi.org/10.1175/WAF-D-16-0141.1.

Kis, A. K., and J. M. Straka, 2010: Nocturnal tornado climatology. *Wea. Forecasting*, **25**, 545–561, https://doi.org/10.1175/2009WAF2222294.1.

Klein, P., and Coauthors, 2015: LABLE: A multi-institutional, student-led, atmospheric boundary layer experiment. *Bull. Amer. Meteor. Soc.*, **96**, 1743–1764, https://doi.org/10.1175/BAMS-D-13-00267.1.

Knuteson, R. O., and Coauthors, 2004a: Atmospheric Emitted Radiance Interferometer. Part I: Instrument design. *J. Atmos. Oceanic Technol.*, **21**, 1763–1776, https://doi.org/10.1175/JTECH-1662.1.

——, and Coauthors, 2004b: Atmospheric Emitted Radiance Interferometer. Part II: Instrument performance. *J. Atmos. Oceanic Technol.*, **21**, 1777–1789, https://doi.org/10.1175/JTECH-1663.1.

Koch, S., and E. N. Rasmussen, 2016: VORTEX-Southeast: Program and activities. *28th Conf. on Severe Local Storms*, Portland, OR, Amer. Meteor. Soc., 3.1, https://ams.confex.com/ams/28SLS/webprogram/Paper300782.html.

Lange, D., J. Tiana-Alsina, U. Saeed, S. Tomás, and F. Rocadenbosch, 2014: Atmospheric boundary layer height monitoring using a Kalman filter and backscatter lidar returns. *IEEE Trans. Geosci. Remote Sens.*, **52**, 4717–4728, https://doi.org/10.1109/TGRS.2013.2284110.

——, F. Rocadenbosch, J. Tiana-Alsina, and S. Frasier, 2015: Atmospheric boundary layer height estimation using a Kalman filter and a frequency-modulated continuous-wave radar. *IEEE Trans. Geosci. Remote Sens.*, **53**, 3338–3349, https://doi.org/10.1109/TGRS.2014.2374233.

Lee, T., M. Buban, and T. Meyers, 2016a: NOAA/ARL/ATDD micrometeorological tower data, version 1.0. UCAR/NCAR–Earth Observing Laboratory, accessed 25 August 2017, https://doi.org/10.5065/d6bg2mbj.

——, ——, and ——, 2016b: NOAA/ATDD mobile radiosonde data, version 1.0. UCAR/NCAR–Earth Observing Laboratory, accessed 25 August 2017, https://doi.org/10.5065/d68k77fn.

Mansell, E. R., C. L. Ziegler, and E. C. Bruning, 2010: Simulated electrification of a small thunderstorm with two-moment bulk

Brought to you by NOAA Central Library | Unauthenticated | Downloaded 08/02/23 01:52 PM UTC

microphysics. *J. Atmos. Sci.*, **67**, 171–194, https://doi.org/10.1175/2009JAS2965.1.

May, R. M., and Coauthors, 2021: MetPy: A Python package for meteorological data. Unidata, accessed 10 February 2020, https://doi.org/10.5065/D6WW7G29.

Mlawer, E. J., S. J. Taubman, P. D. Brown, M. J. Iacono, and S. A. Clough, 1997: Radiative transfer for inhomogeneous atmospheres: RRTM, a validated correlated-k model for the longwave. *J. Geophys. Res.*, **102**, 16 663–16 682, https://doi.org/10.1029/97JD00237.

National Weather Service, 2016: NWS Huntsville Storm Surveys from 03/31/2016. NOAA, accessed 14 August 2016, https://www.weather.gov/hun/hunsur_2016-03-31_surveys#priceville.

NOAA/NWS Storm Prediction Center, 2016: Mesoscale analysis data. NOAA, accessed 13 March 2016, http://catalog.eol.ucar.edu/vortex-se_2016/129/date/2016/03/31.

Noilhan, J., and S. Planton, 1989: A simple parameterization of land surface processes for meteorological models. *Mon. Wea. Rev.*, **117**, 536–549, https://doi.org/10.1175/1520-0493(1989)117<0536:ASPOLS>2.0.CO;2.

NWS Storm Prediction Center, 2016a: Mar 31, 2016 0600 UTC Day 1 Convective Outlook. NOAA, accessed 18 August 2016, https://www.spc.noaa.gov/products/outlook/archive/2016/day1otlk_20160331_1630.html.

——, 2016b: Mesoscale Discussion 310. NOAA, accessed 18 August 2016, https://www.spc.noaa.gov/products/md/2016/md0310.html.

——, 2016c: Mesoscale Discussion 315. NOAA, accessed 18 August 2016, http://www.spc.noaa.gov/products/md/2016/md0315.html.

——, 2016d: Mesoscale Discussion 317. NOAA, accessed 18 August 2016, http://www.spc.noaa.gov/products/md/2016/md0317.html.

——, 2016e: Tornado Watch 72. NOAA, accessed 18 August 2016, http://www.spc.noaa.gov/products/watch/2016/ww0072.html.

——, 2016f: Mesoscale Discussion 311. NOAA, accessed 18 August 2016, https://www.spc.noaa.gov/products/md/2016/md0311.html.

Pleim, J. E., and A. Xiu, 1995: Development and testing of a surface flux and planetary boundary layer model for application in mesoscale models. *J. Appl. Meteor.*, **34**, 16–32, https://doi.org/10.1175/1520-0450-34.1.16.

Rasmussen, E., and S. Koch, 2016: VORTEX-Southeast: Lessons learned and early results. *28th Conf. on Severe Local Storms*, Portland, OR, Amer. Meteor. Soc., 3.2, https://ams.confex.com/ams/28SLS/webprogram/Paper301782.html.

——, and Coauthors, 2015: VORTEX-Southeast Program Overview. National Severe Storms Laboratory Rep., 36 pp., ftp://ftp.atdd.noaa.gov/pub/vortexse/ProjectOverview.pdf.

Sherburn, K. D., and M. D. Parker, 2014: Climatology and ingredients of significant severe convection in high-shear, low-CAPE environments. *Wea. Forecasting*, **29**, 854–877, https://doi.org/10.1175/WAF-D-13-00041.1.

——, ——, J. R. King, and G. M. Lackmann, 2016: Composite environments of severe and nonsevere high-shear, low-CAPE convective events. *Wea. Forecasting*, **31**, 1899–1927, https://doi.org/10.1175/WAF-D-16-0086.1.

Tanamachi, R. L., S. J. Frasier, J. Waldinger, A. LaFleur, D. D. Turner, and F. Rocadenbosch, 2019: Progress toward characterization of the atmospheric boundary layer over northern Alabama using observations by a vertically pointing, S-band profiling radar during VORTEX-Southeast. *J. Atmos. Oceanic Technol.*, **36**, 2221–2246, https://doi.org/10.1175/JTECH-D-18-0224.1.

Tong, M., and M. Xue, 2005: Ensemble Kalman filter assimilation of Doppler radar data with a compressible nonhydrostatic model: OSS experiments. *Mon. Wea. Rev.*, **133**, 1789–1807, https://doi.org/10.1175/MWR2898.1.

——, and ——, 2008: Simultaneous estimation of microphysical parameters and atmospheric state with simulated radar data and ensemble square root Kalman filter. Part I: Sensitivity analysis and parameter identifiability. *Mon. Wea. Rev.*, **136**, 1630–1648, https://doi.org/10.1175/2007MWR2070.1.

Turner, D. D., 2016: OU/NSSL CLAMPS microwave radiometer and surface meteorological data, version 1.0. UCAR/NCAR–Earth Observing Laboratory, accessed 15 October 2016, https://doi.org/10.5065/D6154FFP.

——, and U. Löhnert, 2014: Information content and uncertainties in thermodynamic profiles and liquid cloud properties retrieved from the ground-based Atmospheric Emitted Radiance Interferometer (AERI). *J. Appl. Meteor. Climatol.*, **53**, 752–771, https://doi.org/10.1175/JAMC-D-13-0126.1.

——, and W. G. Blumberg, 2019: Improvements to the AERIoe thermodynamic profile retrieval algorithm. *IEEE J. Sel. Top. Appl. Earth Obs. Remote Sens.*, **12**, 1339–1354, https://doi.org/10.1109/JSTARS.2018.2874968.

Wagner, T. J., P. M. Klein, and D. D. Turner, 2019: A new generation of ground-based mobile platforms for active and passive profiling of the boundary layer. *Bull. Amer. Meteor. Soc.*, **100**, 137–153, https://doi.org/10.1175/BAMS-D-17-0165.1.

Weckwerth, T. M., K. J. Weber, D. D. Turner, and S. M. Spuler, 2016: Validation of a new water vapor micropulse differential absorption lidar (DIAL). *J. Atmos. Oceanic Technol.*, **33**, 2353–2372, https://doi.org/10.1175/JTECH-D-16-0119.1.

Whitaker, J. S., and T. M. Hamill, 2012: Evaluating methods to account for system errors in ensemble data assimilation. *Mon. Wea. Rev.*, **140**, 3078–3089, https://doi.org/10.1175/MWR-D-11-00276.1.

Wulfmeyer, V., and Coauthors, 2015: A review of the remote sensing of lower-tropospheric thermodynamic profiles and its indispensable role for the understanding and simulation of water and energy cycles. *Rev. Geophys.*, **53**, 819–895, https://doi.org/10.1002/2014RG000476.

Xue, M., J. Zong, and K. K. Droegemeier, 1996: Parameterization of PBL turbulence in a multi-scale non-hydrostatic model. Preprints, *11th Conf. on Numerical Weather Prediction*, Norfolk, VA, Amer. Meteor. Soc., 363–365.

——, K. K. Droegemeier, and V. Wong, 2000: The Advanced Regional Prediction System (ARPS)—A multi-scale nonhydrostatic atmospheric simulation and prediction model. Part I: Model dynamics and verification. *Meteor. Atmos. Phys.*, **75**, 161–193, https://doi.org/10.1007/s007030070003.

——, and Coauthors, 2001: The Advanced Regional Prediction System (ARPS)—A multi-scale nonhydrostatic atmospheric simulation and prediction tool. Part II: Model physics and applications. *Meteor. Atmos. Phys.*, **76**, 143–165, https://doi.org/10.1007/s007030170027.

——, D.-H. Wang, J.-D. Gao, K. Brewster, and K. K. Droegemeier, 2003: The Advanced Regional Prediction System (ARPS), storm-scale numerical weather prediction and data assimilation. *Meteor. Atmos. Phys.*, **82**, 139–170, https://doi.org/10.1007/s00703-001-0595-6.

Brought to you by NOAA Central Library | Unauthenticated | Downloaded 08/02/23 01:52 PM UTC